The Origin of Continental Carbonates in Andean Salars: A Multi-Tracer Geochemical Approach in Laguna Pastos Grandes (Bolivia)

E. Muller[1], E. C. Gaucher[2], C. Durlet[3], J.S. Moquet[1], M. Moreira[1], V. Rouchon[4], P. Louvat[1], G. Bardoux[1], S. Noirez[4], C. Bougeault[3], E. Vennin[3], E. Gérard[1], M. Chavez[5], A. Virgone[2], M. Ader[1]

[1]Université de Paris, Institut de physique du globe de Paris, CNRS, F-75005 Paris, France

[2]Total CSTJF, Avenue Larribau, 64018 Pau Cedex, France

[3]Biogéosciences, UMR 6282 CNRS, 6 boulevard Gabriel, Université Bourgogne Franche-Comté, 21000 Dijon, France

[4]IFP Energies Nouvelles, 1-4 Avenue de Bois Préau, 92852, Rueil-Malmaison Cedex, France

[5]Total E&P, 40 Calle Las Violetas, Edificio Arcus, Santa Cruz de la Sierra, Bolivia

Corresponding author: Elodie Muller (emuller@ipgp.fr)

This article has been submitted in November 2018 and is under review in GCA.

Abstract

In continental volcanic settings, abundant carbonate precipitation can occur with atypical facies compared with those of marine settings. The (bio-)chemical processes responsible for their development and early diagenesis are typically complex and not fully understood. In the Bolivian Altiplano, Laguna Pastos Grandes hosts a 40-km^2 carbonate platform composed of a great diversity of carbonate facies mainly fed by thermal springs. It provides for a spectacular natural laboratory for studying carbonate precipitation in a continental province dominated by volcanism. As a first step toward understanding the processes responsible for the precipitation of carbonates in Laguna Pastos Grandes, we will focus on characterizing the fluids (liquid and gas) that feed the laguna. The content of major elements and stable isotope compositions (δ^2H-δ^{18}O, δ^{37}Cl, δ^7Li, δ^{11}B and ^{87}Sr/^{86}Sr) of brine and freshwater inputs were investigated to trace the origin of both water and solutes in the laguna. The stable isotope compositions (δ^{13}C, δ^{15}N) and noble gas isotope ratios of outgassing at the laguna's floor were also determined. The results show that thermal springs are close to saturation with calcite. PHREEQC modeling of the hydrological system, together with gas geochemistry results and temperature estimated from a combination of geothermometers, indicates that Ca in these springs is inherited from the alteration of the volcanic bedrock by aqueous fluids heated at ~225 °C and highly enriched in magmatic mantle-derived CO_2. Our results clearly show that the main driver for the precipitation of modern carbonates in the Central Andes is the deeply sourced CO_2, which boosts the alteration of volcanic rocks at depth.

1. Introduction

Continental volcanic provinces are not known for their abundance in terrestrially formed carbonate deposits. Volcanoclastic, bio-silica, clay or evaporitic sediments are typically dominant. However, it has long been documented that carbonates can also form, in varying abundances, both in pedogenetic profiles (see synthesis in Zamanian et al., 2017; Durand

et al., 2018) and in palustro-lacustro contexts (see synthesis in Alonso-Zarza and Tanner, 2010; Verrecchia, 2017). Such continental carbonates have been generally less studied than marine ones, which have been considered as common hydrocarbon reservoirs and traditional archives for past oceans since the Archean. Yet, the recent discovery of hydrocarbon plays in Lower Cretaceous continental carbonates off the Brazilian coast helped change that view (Terra et al., 2010; Tosca and Wright, 2015) and promoted various and numerous studies into the origin and occurrence of carbonates in continental areas where the catchment and underlying rocks are mainly volcanic (Teboul et al., 2016; 2017).

Laguna Pastos Grandes in southern Bolivia exhibits a ~40 km^2 recent to modern carbonate platform making it unique among the more than 200 salars scattered across the volcanic Central Andes region (Fig. 1a, b). Laguna Negra in Argentina is the only other Andean salar recently described with a significant, but much smaller (6.5 km^2; Gomez et al., 2014), carbonate platform. Laguna Pastos Grandes exhibits a great diversity of calcitic, siliceous and evaporitic fabrics deposited in palustrine to shallow lacustrine environments, including some of the largest modern pisoliths discovered to date (Fig. 1c; Risacher and Eugster, 1979; Jones and Renaut, 1994; Bougeault et al., 2019). In some ways, it may be considered as a modern equivalent of carbonate facies and processes that occurred during sedimentation of the Presalt facies in the volcanic-rich South Atlantic realm during the Early Cretaceous.

Despite several studies already conducted on the hydrology and origin of chemical sediments in Bolivian and Chilean salars, no clear evidence appears to explain the abundance of modern carbonates in Laguna Pastos Grandes. From structural, hydrological and lithological points of view, this seems to occur in similar environments than salars where carbonates are absent or not modern (Risacher et al., 2003; Risacher and Fritz, 2009; see geological setting). Although climatic parameters fundamentally control the existence and morphology of salars (Risacher and Fritz, 2009), the chemical composition of the brines and the nature of the precipitates in these lakes depend on the initial composition of the inflow waters. In the present study, we thus performed a comprehensive geochemical study of gases and waters discharging in the carbonate platform of Laguna Pastos Grandes and brine filling the main basin.

The overarching goal of our research is to better understand the ongoing processes that allow for the rapid growth of these continental carbonates in a volcanic area under structural extension and fed by hydrothermal fluids. As a first step, this study focuses on the origin of the fluids and solutes from which carbonates have formed in the laguna based on the study of: (i) the chemical compositions of both water samples from streams of the drainage area and hydrothermal springs upwelling through or near the carbonate platform and gas associated with the hydrothermal springs; (ii) the isotopic compositions of gas components ($\delta^{13}C$, $\delta^{15}N$ and noble gases), water samples ($\delta^{2}H$ and $\delta^{18}O$) and some of their solutes ($\delta^{37}Cl$, $\delta^{7}Li$, $\delta^{11}B$ and $^{87}Sr/^{86}Sr$); and (iii) Li, B and Sr isotopic compositions of volcanic rock samples surrounding the salar. These results, together with the temperature of the underlying geothermal reservoir estimated from a combination of geothermometers and PHREEQC modeling of the hydrological system allowed us to discuss the main factors

responsible for the high precipitation of modern carbonates in Laguna Pastos Grandes compared with the other Andean salars.

2. Geological Setting

Laguna Pastos Grandes is located in the southern part of the Bolivian Altiplano, in the South Lipez region. The Altiplano (3700 – 4500 m) is a major Plio-Pleistocene continental plateau bounded by the Eastern and Western Cordilleras and dominated by Cenozoic stratovolcanoes and their products (Fig. 1). To the south, rhyolitic ignimbrites and dacites to rhyodacites of the Altiplano-Puna Volcanic Complex (APVC) dominate the South Lipez region, whereas andesites to dacites predominate on the Chilean side (Thorpe et al., 1976). Native sulfur deposits occur on many of the volcanoes in Chile, and thermal springs are abundant. A thick succession of Cretaceous and Tertiary continental sediments, including evaporite deposits, has been observed in the Bolivian Eastern Cordillera and could be covered by volcanic rocks toward the west in the studied area (Kussmaul et al., 1977; Deconinck et al., 2000).

There are more than 200 closed basin lakes in the Bolivian Altiplano and Chilean Western Cordillera (Ericksen and Salas, 1987; Luddington et al., 1992). Most are saline and encompass a wide range of perennial or ephemeral lakes, locally termed “salars”. The two largest salars, Uyuni and Coipasa, are remnants of larger Pleistocene lakes and occupy the lower part of the Altiplano (3650 m altitude), whereas an abundance of smaller evaporitic basins (<400 km^2) occur at higher elevations (4000–4500 m) of the southern Altiplano (Fig. 1). The presence of these southern basins and their morphology are firstly due to the cold and dry climate of this region with a mean annual precipitation of 100-200 mm (Iltis et al., 1984) that mostly falls in summer (December-March); air temperatures ranging from -30 °C in winter (May-August) to 25 °C in summer with daytime fluctuations of up to 40 °C (Risacher and Fritz, 1991); high insolation; and annual evaporation of approximately 1400 mm (Servant-Vildary and Roux, 1990). Although they belong to relatively similar environments in terms of geology and climate, they show a large variety of brine compositions, which can be organized into three major groups: alkaline, sulfate-rich, and calcium-rich brines (Risacher and Fritz, 2009). Different precipitates can be found in association with these brines, the most common being sodium chloride; sodium sulfates to borates; sodium carbonates; and calcium sulfates (Ahlfeld, 1956; Ahlfeld and Branisa, 1960). Their formation and evolution have been suggested to result from the combination of two basic factors: the presence of interior drainage basins as a source of solutes and high rates of evaporation implying salt deposition (Risacher et al., 2003). Inflows to the Andean salars stem from a variety of sources such as permanent and ephemeral streams; shoreline springs; groundwater discharge; and thermal springs. Most of the rainwater falling on the drainage area infiltrates and recharges underlying aquifers. Shoreline spring and hot-spring waters are typically enriched in solutes compared with streams due to the dissolution of ancient and/or present-day evaporitic sediments or by the infiltration and recycling of lake brines. Therefore, the composition of inflow waters feeding Andean salars reflects a mixture from two main sources: (1) dilute waters produced by the alteration of volcanic rocks by meteoric waters and (2) brackish, highly concentrated waters derived from brine/salt recycling (Risacher et al., 2003 and references therein). The high rate of evaporation of these inflow waters in ponds and lakes increases the concentration of solutes and leads to the deposition of a sequence of minerals in the order of their increasing

129 solubility, following diverse evaporative pathways depending on the initial chemistry of
130 inflow waters (Risacher and Fritz, 2009).
131
132 With an area of ~120 km^2, Laguna Pastos Grandes is one of the largest salars of the
133 southern Altiplano (Risacher and Eugster, 1979). This salar lies at an elevation of 4450 m
134 in a 50-km-long caldera dated at 2.89±0.01 Ma by $^{40}Ar/^{39}Ar$ on sanidine (Salisbury et al.,
135 2011) and is probably the remnant of a larger lake that once occupied the caldera moat (de
136 Silva and Francis, 1991). The drainage basin (660 km^2) is limited to the west by rhyolitic
137 lava ridges up to an elevation of 5800 m, and to the east by rhyolitic ignimbrite ridges up
138 to an elevation of 5000 m (Fig. 1b). Coalescent alluvial fans with thin pebbly soils and
139 xerophytic vegetation surround the laguna. Laguna Pastos Grandes can be divided in two
140 main domains previously identified by Ballivian and Risacher (1981) and Jones and Renaut
141 (1994): the eastern domain corresponds to a playa environment characterized by gypsum
142 and carbonate muds associated with ulexite ($NaCaB_5O_6(OH)_6$), and the western domain
143 corresponds to a vast 40-km² palustrine carbonate platform, highly fragmented through
144 cryoturbation exposing underlying recent carbonates (muds to calcarenites). Over these
145 recent carbonate deposits, a few ponds with a depth of no more than a decimeter are
146 characterized by pisoliths and carbonate concretions reaching up to 20 cm (Fig. 2).
147 Hydrothermal springs discharge over this platform producing important modern carbonate
148 deposits (Bougeault et al., 2019).

149 **3. Materials and Methods**

150 **3.1 Water, gas and rock sampling**

151 Nine water samples were collected during two sampling trips in January 2016 and
152 March 2017, dry and wet seasons, respectively (Tables 1, 2). We thus consider our samples
153 as representative of the two main climatic seasons in terms of rainfall. We collected seven
154 samples of water from five thermal springs including one on the border of the laguna; two
155 samples from cold streams; and one sample of brine from the southwestern part of the
156 laguna (Fig. 2, Tables 1, 2). Water samples were filtered at 0.1 µm with a sterile acrylic
157 filter (Sartorius Minisart®) fixed at the end of a 50 mL syringe and cation samples were
158 acidified with HNO_3 in the field. The temperature and pH were measured on site at each
159 collection point. The alkalinity was determined by HCl titration and Gran's plotting
160 immediately after sampling and filtration in 2016 (Table 2) and for the 2017 samples, by
161 end-point titration with H_2SO_4 at the Total laboratory (France). Two samples of fresh snow
162 and one sample of rainfall were also collected respectively in January 2016 and March
163 2017 in order to constrain the meteoric sources of water in the area (Table A2).
164
165 Four thermal springs named *La Salsa*, *La Rumba*, *El Ojo Verde* and *El Gigante*
166 (Fig. 2) were selected for both water and gas sampling on the carbonate platform based on
167 accessibility and high water-gas flux. *La Salsa*, *La Rumba* and *El Ojo Verde* springs contain
168 bubbling sources of gas in water ponds whereas *El Gigante* is a dry source of gas (a mofet)
169 away from the main water source. Gases were only collected in March 2017 in 100- and
170 250-mL stainless-steel reservoirs and in four 12 mL Exetainer® vials, all previously
171 evacuated to primary vacuum. To capture bubbling thermal spring gases, an inverted funnel
172 connected to a rubber pipe was submerged in spring water and placed on top of the rising
173 bubbles (Fig. A1). The other end of the pipe was then connected through a T-junction to a
174 stainless-steel fitting ending in a septum (for sampling in an Exetainer®) and a stainless-

steel reservoir (for direct sampling) connected to a GA5000 gas detector (Scientific Instruments). Before collecting the gases accumulated in the funnel, the sampling system was completely flushed by the continuously outgassing bubbles to avoid air contamination. The O_2 level at the outlet of the sampling system was continuously monitored with the gas detector to ensure limited air contamination during sampling. The gas was collected when O_2 levels stabilized at the lowest level (typically below 2.0%).

Five rock samples representative of the volcanic bedrock were also collected on the border of the laguna. These included two andesites, two dacites and one ignimbrite of rhyolitic composition (see location in Fig. 2).

3.2 Analytical methods – Chemical compositions

Gas composition

The composition of the gas was determined on the four samples (100, 112, 116, 117) collected in Exetainer® vials with a Varian 3800 high-resolution gas chromatograph (GC) at the IFPEN laboratory (Rueil-Malmaison, France). This GC is equipped with several columns, two thermal conductivity detectors (TCD) and one flame-ionization detector (FID) operating under He and N_2 as carrier gases. The quantification of H_2 and He was realized on one TCD with N_2 as the carrier gas, whereas CO_2, N_2, O_2 and CH_4 were analyzed using the other TCD with He as the carrier gas. Relative concentrations were calculated after the chromatographic response had been calibrated in partial pressure for each compound using the specific external standards "Air Liquide TM" and "Saphir". These standards are quality gas mixtures that include H_2, He, N_2, CO_2, O_2, CH_4, C_2H_6, C_3H_8, n-C_4H_{10} and i-C_4H_{10} and are available in the laboratory at different concentrations to cover the specific sample compositions. Each analysis was bracketed with blanks. Results are given with a precision of ± 5 vol.% for O_2, ±1.3 vol.% for CO_2, ±3 vol.% for N_2 and ±0.1 vol.% for CH_4 based on repeated measurements of gas standards in similar concentrations.

Water composition

All chemical analyses were carried out in the Total laboratories (Pau, CSTJF, France) using ion chromatography (Cl, Br and SO_4); Inductively Coupled Plasma-Atomic Emission Spectroscopy (Li, B and Sr); Inductively Coupled Plasma-Mass Spectrometry (Ca and Mg); Flame Emission Spectrometry (Na, K, Ca and SiO_2); and titration (alkalinity). The accuracy of the determination of major species was better than ± 5% and verified by repeated measurements of standard materials, namely Ion96-3 and LGC6020 for cations and anions, and pure Li and B standard solutions (Merck) for Li and B determinations. Saline samples were analyzed either after dilution (to minimize matrix effects during measurement) or by using the technique of adding a standard (to match the matrixes of the standard materials). The matrix effects were validated on at least three dilutions (500, 1000, 2000).

3.3 Analytical methods – Isotopic compositions

CO_2 gas

The isotopic composition of the CO_2 was measured in samples contained in Exetainer® vials at the IFPEN laboratory using a MAT253 (Finnigan Mat-Thermo Fisher) triple collection mass spectrometer coupled to a gas chromatograph, operating with He as a carrier gas. The internal reference CO_2 gas was calibrated with the international gas

reference standards RM8562, RM8563 and RM8564 with $\delta^{13}C_{vPDB}$ of -3.76 ± 0.03 ‰, -41.56 ± 0.04‰ and -10.45 ± 0.03‰, respectively (Verkouteren and Klinedinst, 2004). All the isotopic compositions given in this study are reported in the usual δ-scale in‰ according to δ_{sample} (‰) = {($R_{sample}/R_{standard}$) -1} x 1000, where R is the $^{13}C/^{12}C$ atomic ratio. The uncertainties on $\delta^{13}C$ values are better than ± 0.4‰ based on the external reproducibility of internal standards.

N_2 gas

The isotopic composition of N_2 was measured at the Institut de physique du globe de Paris (IPGP, France) on the gas captured in Exetainer® vials or stainless-steel cylinders. The N_2 was purified and isolated from other gases before being transferred to the IRMS dual-inlet mass spectrometer Delta + XP (Finnigan Mat-Thermo Fisher) for isotopic analyses. N_2 purification was performed using the high vacuum line ($P<10^{-5}$ mbar) described in Li et al. (2009). Purification starts with a cryogenic separation at liquid nitrogen temperature. The non-condensable gases, including N_2, H_2, O_2, CH_4 and He, are inserted in the line and circulated using a mercury Toeppler pump through a CuO reactor maintained at 950 °C for 30 minutes (and then cooled to 450 °C) to oxidize H_2 and CH_4. The resulting CO_2 and H_2O are cryogenically trapped at liquid-nitrogen boiling temperature. Excess O_2, if any, is resorbed and the NOx that was potentially generated during the previous oxidation phase is reduced to N_2 by circulating the gases over a Cu reactor maintained at 600 °C. The purified N_2 and He are then collected with the mercury Toeppler pump and manometrically quantified before being transferred in vials for measurement using a dual-inlet IRMS Delta + XP. This instrument is calibrated by measuring an internal reference N_2 gas, itself calibrated against the air, the international reference standard for $\delta^{15}N$ measurements, which has by definition an absolute value of $\delta^{15}N_{Air}$ = 0‰. We obtained a relative uncertainty on the $\delta^{15}N$ better than ± 0.5‰ taking into account the N_2 extraction process efficiency and the reproducibility on internal standards.

The CO_2 that was trapped using liquid nitrogen was then released at -140 °C, collected using a liquid N_2 trap and manometrically quantified before being transferred to vials for measurement using the dual-inlet IRMS Delta + XP. $\delta^{13}C$ values compare well with those obtained by GC/C/IRMS at the IFPEN laboratory (Table A1).

Noble gases

Following the protocol of Moreira et al. (2018), noble gas isotopic compositions were measured in gas samples (100, 112, 116, 117) at IPGP using the Helix-SFT (Split Fight Tube, Thermo Instruments©). In brief the gas purification consists of several combustions: the first one with a Bulk Getter (SAES) heating system maintained at 400 °C for 5 minutes, followed by two 5-minute combustions at 800 °C each with titanium sponge. After purification, helium is separated from the other noble gases using activated charcoal at 30 K, introduced into the Helix-SFT mass spectrometer and analyzed using peak jumping. ^3He is collected on the electron multiplier in pulse-counting mode whereas ^4He is analyzed on the Faraday cup and the signal is amplified using either 10^{11} ohm or 10^{12} ohm resistance depending on the signal. After the helium has been measured, neon is released from the cold trap at 70 K. Two cycles of neon isotope measurement are performed before neon is introduced to stabilize the magnet. For each cycle, ^{20}Ne is measured using a mass-scan instead of setting the magnet on the required field to measure ^{20}Ne (see Moreira et al., 2018 for details). ^{21}Ne, ^{22}Ne, ^{40}Ar and CO_2 were measured for 10 seconds each using peak switching. Argon is partially desorbed at 130 K and transferred to charcoal at the

temperature of liquid nitrogen for 15 minutes. After the desorption of argon at room temperature from the charcoal trap, dilution(s) using a 1 L balloon is/are used to decrease the amount of argon introduced into the mass spectrometer. ^{36}Ar and ^{38}Ar are collected on the electron multiplier, whereas ^{40}Ar is measured on the Faraday cup using 10^{11} ohm resistance. All the data were corrected following the procedure of Moreira et al. (2018). For Ne and Ar, the standard is the atmosphere. The helium standard is a gas collected at the Irene thermal spring (Reunion island) with a $^{3}He/^{4}He$ value of 12.56 ± 0.05 R_A. For the present study, blank corrections were negligible. Final uncertainties for the isotopic ratios in samples are ±0.1 for R/Ra, ±0.06 for $^{20}Ne/^{22}Ne$, ±0.0005 for $^{21}Ne/^{22}Ne$, ±5 for $^{40}Ar/^{36}Ar$ and correspond to the error propagation of the measured uncertainty, the blank correction, and the correction for mass discrimination.

Water isotopes

Oxygen and hydrogen isotope measurements were performed at BRGM's stable isotope laboratory by equilibrating 1 mL of water with gas mixtures of H_2–He and CO_2–He respectively for δ^2H and $\delta^{18}O$, for one night and using a Finnigan MAT 252 mass spectrometer (Assayag et al., 2008). The external precision was ± 0.1‰ for $\delta^{18}O$ and ± 0.8‰ for δ^2H vs. SMOW.

Chlorine

The chlorine stable isotope compositions were measured at the IPGP on gaseous CH_3Cl that was prepared and purified with the method described in Godon et al. (2004). The $\delta^{37}Cl$ measurements were then performed on the dual-inlet IRMS Delta + XP. They are reported in Table A3 with the conventional $\delta^{37}Cl$ notation in per mil variations relative to Standard Mean Ocean Chlorine (SMOC, Godon et al., 2004). During the course of this study, the external reproducibility of the seawater standard was 0 ± 0.04‰ (1s, n = 18) as routinely obtained at IPGP for more than two decades now (Godon et al., 2004; Bonifacie et al., 2005; Giunta et al., 2015). Four pore fluid samples were measured twice. The mean difference value between duplicates was 0.04‰.

δ^7Li analysis

In water samples, lithium isotopic compositions were measured using a Neptune Multi Collector ICP-MS (Thermo Fisher Scientific) at BRGM's stable isotope laboratory. $^7Li/^6Li$ ratios were normalized to the L-SVEC standard solution (NIST SRM 8545, Flesch et al., 1973) following the standard-sample bracketing method (see Millot et al., 2004 for more details). The uncertainties on δ^7Li values are better than ± 0.5‰ (2σ) based on the external reproducibility using internal standards (seawater IRMM BCR-403 and basalt JB-2).

In volcanic rocks, Li was separated from the matrix by ion-exchange chromatography using the method described in detail by Dellinger et al. (2015). In brief, after digestion, a sample aliquot was loaded onto a column filled with AG50-X12 resin and the Li was eluted in HCl 0.2 N. The Li isotopic composition was measured by MC-ICP-MS Neptune (Thermo Scientific, Bremen) at IPGP using an APEX desolvating system and at typical Li concentrations of 20–30 ppb. Each sample was successively measured three times within a standard-sample bracketing (SSB) sequence, yielding five δ^7Li values from which an average value was derived. Data were corrected for the background intensities recorded before each bracketing standard and each sample. The intensity of the background was no more than 0.5–1% of the sample intensity. The overall reproducibility and accuracy

of the procedure (including solid sample digestion and Li separation) was checked by measurement of the basalt reference material BHVO-2 (δ^7Li = 4.23 ± 0.83‰; Ryu et al., 2014). The external error (2σ) was better than 0.5‰. Finally, the concentration of the total procedural blank (acid digestion and column chemistry) was assessed to be less than 0.05 ng, i.e., insignificant compared with the amount of Li in the samples. The results are given in Table 4.

δ^{11}B analysis

In water samples, boron isotopic compositions were determined on a Finnigan MAT 261 solid source mass spectrometer in a dynamic mode at BRGM's stable isotope laboratory. For these samples, water volumes corresponding to a mass of 10 µg of B underwent a two-step chemical purification using Amberlite IRA-743 selective resin according to a method adapted from Gaillardet and Allègre (1995). The uncertainties on δ^{11}B values are better than ± 0.3‰ (2σ) based on the external reproducibility using the internal standard NBS951 (δ^{11}B = 4.05398 ± 0.00105‰).

Rock samples were dissolved by alkali fusion and B was extracted following the procedure of Chetelat et al. (2009). 50 mg of finely powdered sample were admixed with 300 mg of ultra-pure K_2CO_3 in a Pt crucible and melted in a muffle furnace at 950 °C for 15 minutes. The pellet was taken up in 3 mL of 0.5 HNO_3 and added to a 50 mL vial filled with 20 mL H_2O. An additional 1-2 mL of 0.5N HNO_3 were added until complete dissolution. The final pH was adjusted to pH 1.7 with 3N HNO_3, and 7 mL of this solution were passed through 2 mL of the cation exchange resin AG 50W-X8 to extract most of the cationic load. The recovered solution was adjusted to pH 8-9 with distilled 4N NH_4OH and B was extracted on Amberlite IRA-743 resin (adapted from Lemarchand et al., 2002) in two steps: the first step consisted of extraction on a column loaded with 300 µL of resin and the second step of purification (after adjustment to pH 8-9 again) on a column filled with 50 µL of the resin. Boron isotope ratios were determined by MC-ICP-MS with a direct injection nebulizer (d- DIHEN; Louvat et al., 2014) at IPGP with a 2σ reproducibility between 0.05 and 0.3‰. $^{11}B/^{10}B$ values are expressed relative to the boric acid standard NBS 951 (NIST). The results are given in Table 4.

$^{87}Sr/^{86}Sr$ measurement

In water samples, chemical purification of Sr (~3 µg) was done using an ion-exchange column (Sr-Spec) before mass analysis according to a method adapted from Pin and Bassin (1992) with total blank <1 ng for the entire chemical procedure. After chemical separation, around 150 ng of Sr were loaded onto a tungsten filament with tantalum activator and analyzed with a Finnigan MAT 262 multi-collector mass spectrometer at BRGM's stable isotope laboratory. The $^{87}Sr/^{86}Sr$ values were normalized to the certified value of the NBS987 standard 0.710240. An average internal precision of ± 10 ppm (2σm) was obtained and the reproducibility of the $^{87}Sr/^{86}Sr$ ratio measurements was verified by repeated analysis of the NBS987 standard ($^{87}Sr/^{86}Sr$ = 0.710243 ± 10, 2σ).

After total evaporation of ~0.2 mL of rock sample digestion solutions, the remaining solid was retaken with 0.1 mL of HNO_3 3N and loaded onto a Sr-SPEC (Eichrom) resin chromatography column to separate ca. 200 ng of Sr (Pin and Bassin, 1992). The Sr isotopic composition was measured by MC-ICP-MS at the IPGP. The mass discrimination was corrected using the invariant ratio $^{88}Sr/^{86}Sr$ (0.1194). Accuracy and reproducibility were verified by repeated analysis of the NBS standard SRM 987 ($^{87}Sr/^{86}Sr$ = 0.710250±0.0000025). The results are given in Table 4.

3.5 PHREEQC modeling

The PHREEQC software, version 3 (Parkhurst and Appelo, 2013) was applied to compute aqueous speciation and fluid-mineral equilibria using the "thermoddem v1.10 06jun2017" thermodynamic database (website http://thermoddem.brgm.fr/; Blanc et al., 2012).

4. Results

4.1 Gas molecular and noble gases composition

Table 1. Analytical results of the gas sampled in 2017: bubbling gas from La Salsa, La Rumba and El Ojo Verde spring sources and dry gas from El Gigante gas source. $\delta^{15}N$ and $\delta^{13}C$ values are averaged from multiple measurements (n=2-6) except for sample PG17_116, which was analyzed only once for $\delta^{15}N$ (see Table A1 for detailed nitrogen and carbon isotopic analyses). See text for calculations of atmospheric N_2 proportion, $\delta^{15}N$ correction from atmospheric contribution and modeling results.

Sample no.	PG17_100	PG17_112	PG17_116	PG17_117
Sample location	La Salsa	La Rumba	El Gigante	El Ojo Verde
Latitude (°S)	21.619349	21.638776	21.64819	21.651306
Longitude (°W)	67.848462	67.852883	67.848736	67.840695
Temperature (°C)	43.4	44.6	41.5	36.2
Major composition (vol.%)				
CO_2	74.7	66.2	86.0	38.4
CH_4	0.04	0.03	0.00	0.07
O_2	3.36	2.01	1.63	4.76
N_2	21.8	32.0	12.4	56.4
% N_2	57.3	23.4	49.1	31.5
Isotopic composition (‰)				
$\delta^{13}C$ (±0.1‰, 2σ)	-11.2	-11.2	-11.2	-11.0
$\delta^{15}N$ (±0.5‰, 2σ)	2.7	1.8	1.6	2.3
$\delta^{15}N_{primary}$	6.4	2.3	3.1	3.4
Noble gases (ppm)				
^{4}He	337	517	109	814
^{20}Ne	0.561	1.498	0.425	2.033
^{36}Ar	7.089	12.865	3.575	12.169
$^{40}Ar/^{36}Ar$	298	288	283	288
R_C/R_A	3.68	3.84	3.81	3.86
Mantle He (%)	45.4	47.3	47.1	47.6
$CO_2/^{3}He_{surface}$	$4.35*10^8$	$2.42*10^8$	$1.51*10^9$	$8.85*10^7$
Modeling				
$CO_2/^{3}He_{before\ degassing}$	$1.2*10^8$	$9.6*10^8$	$2.9*10^9$	$4.7*10^8$
CO_2 exsolution (%)	36	23	49	17

The gas from thermal springs is mainly composed of CO_2 (38.4 to 86 vol. %) and N_2 (12.4 to 56.4 vol. %) with minor amounts of O_2 (1.63 to 4.76 vol. %) and negligible traces of CH_4 (< 0.07 vol. %; Table 1, Fig. 2). No H_2 and H_2S were detected. If we assume that O_2 is derived from atmospheric contamination during sampling or natural diffusion into the thermal spring from the surface, we can calculate a contribution of associated atmospheric N_2 up to 57.3% of the total N_2 (Table 1). The air-normalized abundances of the

Atmosphere-Derived Noble Gases (ADNG: ^{20}Ne and ^{36}Ar) display depleted values compared with air that follow the composition of the Air Saturated Water (ASW; Fig. 3). In contrast, ^{4}He is found in high proportions, from 109 to 814 ppm, displaying a high $^{3}He/^{4}He$ value normalized to air (R_C/R_A) of 3.79 ± 0.08 on average (with $(^{3}He/^{4}He)_{air}$ = $1.4x10^{-6}$; Table 1). This value indicates a high mantle contribution (Sano and Marty, 1995, see discussion).

4.2 Gas C and N isotope compositions

The CO_2 gas sampled from thermal springs shows homogeneous $\delta^{13}C$ values with an average of -11.1 ± 0.1‰ (Table 1, A1). In contrast, the isotopic composition of N_2 ($\delta^{15}N$) is more variable and ranges between 1.6 and 2.7 ± 0.5‰. Nitrogen isotope measurements of sample PG17_112 were performed on gases sampled in both Exetainers® and stainless-steel tubes to ensure a good reproducibility of the results, regardless of the container used (Table A1). Considering an atmospheric contamination of up to 57.3% for N_2, we can estimate the primary $\delta^{15}N$ value by isotopic mass balance as follows:

$\delta^{15}N_{measured} = \delta^{15}N_{atm} *\%_{atm} + \delta^{15}N_{primary}*(1-\%_{atm})$

With atmospheric contamination $\%_{atm}$ up to 0.573 and $\delta^{15}N_{atm}$ = 0‰, we obtain a maximum $\delta^{15}N_{primary}$ of 6.4‰ (Table 1). We thus consider the measured values as minimal values.

4.3 Isotopic composition of water

Table 2. Chemical and isotopic data for Laguna Pastos Grandes waters. NICB: Normalized Ionic Charge Balance.

Sample no.	PG17-117	PG17-112	PG17-100	PG1_1	MV_1	PGS_1	PG17_99	SP_3	LS_4
Sampling trip	2017	2017	2017	2016	2016	2016	2017	2016	2016
Name	El Ojo Verde spring	La Rumba spring	La Salsa spring	La Salsa spring	El Gigante spring	Piedmont spring	Stream	Stream	Lake brine
Lat. (°S)	21.651306	21.638776	21.619349	21.61934	21.64865	21.61996	21.60764	21.69665	21.69552
Lg. (°W)	67.840695	67.852883	67.848462	67.84842	67.84866	67.85628	67.75753	67.8098	67.80927
T (°C)	36.2	44.6	43.4	42.2	45.7	32.4	17.3	16.4	24.5
pH	6.41	5.99	6.90	6.42	6.20	6.35	9.15	7.99	7.39
Alkalinity on site				10.7	8.91	4.35		0.78	
Chemical composition (mM)									
Na	232	137	173	220	251	23.7	0.57	1.17	3924
K	12.9	8.7	12.5	13.4	16.6	1.8	0.14	0.36	131
Ca	10.9	6.5	10.1	11.4	12.8	0.7	0.17	0.37	59.7
Mg	5.8	2.8	5.2	5.4	6.0	0.4	0.13	0.18	54.6
Alkalinity	7.4	5.3	7.4	7.4	8.9	1.8	0.90	0.79	10.9
SO_4	2.9	2.3	2.3	2.9	4.2	0.8	0.04	0.22	39.5
Cl	278	173	197	258	291	25.5	0.73	1.52	4375
Li	11.1	6.6	9.9	7.7	9.6	0.8	0.02	0.25	74.8
Sr	0.11	0.06	0.11	0.11	0.15	0.01	0.001	0.003	1.03
B	3.6	2.2	3.3	3.2	4.7	0.5	0.04	0.08	28.6
Br	0.073	0.046	0.069	0.060	0.070	0.006	0.006	0.006	0.426
SiO_2*	116	101	116	155	152	101	36	60	60
Salinity**	16.2	10.1	11.5	15.1	17.0	1.49	0.04	0.09	256
NICB (%)	-1.3	-7.5	6.9	0.7	2.2	-3.1	-26.4	3.0	-2.9
pCO_2 (mbar)***	141	309	60.3	110.0	389.0	61.7	0.03	0.5	10.5
Isotopic compositions (‰ ±2s)									

δ^2H (±0.8)	-92.2	-96.7	-93.9	-93.8	-92.5	-104.2	-99.4	-104.7	7.6
$\delta^{18}O_{H2O}$ (±0.1)	-11.4	-12.4	-11.8	-11.7	-11.4	-14.2	-13.1	-13.2	3.3
δ^7Li	5.2 ±0.1	5.6 ±0.1	3.8 ±0.1	3.6 ±0.1	4.0 ±0.2	2.6 ±0.2	4.0 ±0.2	10.9 ±0.1	3.9 ±0.3
$\delta^{11}B$	-4.4 ±0.1	-5.0 ±0.1	-4.9 ±0.2	-4.3 ±0.3	-6.7 ±0.3	-6.0 ±0.3		0.0 ±0.3	-7.2 ±0.3
$^{87}Sr/^{86}Sr$	0.708384	0.708412	0.708398	0.708396	0.708402	0.708354	0.707950	0.707646	0.708327
$2s_m$	0.000005	0.000006	0.000010	0.000007	0.000006	0.000006	0.000010	0.000007	0.000007

**mg/L; **g/L; ***calculated with PHREEQC based on water chemistry*

Spring waters exhibit a narrow range for $\delta^{18}O$ (-14.2 to -11.4‰) and δ^2H (-104.2 to -92.2‰) and slightly more enriched in ^{18}O and ^2H than streams (with $\delta^{18}O \sim -13.2$‰ and $-104.7 < \delta^2H < -99.4$‰; Fig. 4, Table 2). They are on the regional Ground and Spring Water Line (LGSWL; $\delta^2H = 7.99 \times \delta^{18}O + 0.3$; n = 44) established by Fritz et al. (1981) and Rissmann et al. (2015) to the right of the Local Meteoric Water Line (LMWL) defined for modern precipitation in the Chilean and Bolivian Altiplano at altitudes of 2800 to 5700 m: $\delta^2H = 8.15 \times \delta^{18}O + 15.3$ (Chaffaut et al., 1998). Both streams and springs define a trend modeled by the following equation: $\delta^2H = 4.29 \times \delta^{18}O + 43.8$ ($R^2 = 95$ %, n = 8; Fig. 4b) with more positive $\delta^{18}O$ and δ^2H values than rainfall collected at the altitude of the aquifer system (i.e., at an altitude of 4500 m) during the wet season in March 2017. Two samples of snow collected during the dry season in January 2016 show more positive $\delta^{18}O$ and δ^2H values than rainfall and fall to the left of the LMWL trend (Table A2). The Piedmont thermal spring, located on the border of the laguna, is shifted from the other springs toward more negative $\delta^{18}O$ and δ^2H values. In the southeastern part of Laguna Pastos Grandes, the brine sampled from the southeastern lake (LS4 sample) is enriched in both ^{18}O and ^2H compared with the different inlet waters and shows even greater $\delta^{18}O$ and δ^2H values than other Andean salars on average (Fig. 4, Table A2).

4.4 Geothermometry

Table 3. Estimated equilibrium temperatures (°C) for hydrothermal sources obtained with different geothermometers.

Geothermometer	**PG17_117**	**PG17_112**	**PG17_100**	**PG1_1**	**MV_1**	**PGS_1**
SiO_2 (Verma and Santoyo, 1997)	145	138	145	163	162	138
Na/K/Ca – Mg (Fournier and Potter, 1979)	177	144	169	167	171	107
Na/K (Verma and Santoyo, 1997)	215	226	237	222	230	240
Na/K (Santoyo and Diaz-Gonzalez, 2010)	188	202	216	197	221	207
Na/Li (Fouillac and Michard, 1981)	315	316	344	272	283	268
Na/Li (modified by Sanjuan et al., 2014)	264	264	285	230	239	226
Na/Li (Verma and Santoyo, 1997)	323	324	351	280	292	276
Na/Li (Kharaka et al., 1982)	334	335	353	304	312	301
Na/Li (modified by Sanjuan et al., 2014)	336	337	355	306	314	303
Mg/Li (Kharaka and Mariner, 1989)	199	193	197	185	192	151

The thermal waters associated with gases reach the surface at up to 46 °C, which is among the highest temperatures recorded in the Altiplano salars (Risacher and Fritz, 1991; Spiro et al., 1997). Considering the concentrations of some soluble elements (Si, Na, K, Ca, Mg, Li) in the thermal springs, it is possible to calculate temperatures of the fluids based on empirical, semi-empirical and experimental relations derived from known or unknown equilibrium relations between water and minerals taking place in the geothermal reservoirs (Sanjuan et al., 2014 and references therein). For example, the silica concentration of our

samples is fairly uniform within the range of 101 to 154 mg/l (Table 2). Applying the quartz geothermometer described in Kharaka and Mariner (1989), Verma and Santoyo (1995, 1997) estimated equilibrium temperatures of spring water with the rocks of a deep reservoir up to 163 ± 3 °C (assuming no steam loss; Table 3) with a mean of 149 °C. This estimate decreases by less than 9 °C if we consider adiabatic cooling of the fluid by steam loss after leaving the reservoir (Kharaka and Mariner, 1989). This small shift supports the idea that the original silica concentration in the fluid was only slightly affected by boiling and/or dilution (Cortecci et al., 2005). However, considering the contrast in temperature between the surface and the deep reservoir, a precipitation of silica during the cooling of the water as it ascends to the surface is easy to hypothesize. This loss will minimize the geothermometer based on the silica concentration. The Na-K-Ca geothermometer yields similar estimates (156 °C) with a maximum shift of ± 30 °C when the Mg correction of Fournier and Potter (1979) is applied. However, this geothermometer is calibrated on silicates and can also be affected by a precipitation of silicates during the cooling of the thermal water.

The Na-Li geothermometer gives much higher estimates (around 300 °C) regardless of the equation used (Fouillac and Michard, 1981; Kharaka et al., 1982; Verma and Santoyo, 1993, 1997). Using a larger dataset than in the original articles, Sanjuan et al. (2014) modified the equations of Kharaka et al. (1982) and Fouillac and Michard (1981). These corrections do not modify the results for the Kharaka et al. equation (mean value 325 °C) but decrease the values obtained with the Fouillac and Michard equation (mean value 251 °C) by 50 °C. The Li-Mg geothermometer (Kharaka and Mariner, 1989) yields lower values (~186 °C on average; Table 3) than the Na-Li geothermometer. The discrepancies observed between the geothermometers using Li can be explained by the high concentrations of Li in our samples. The Log(Na/Li) values obtained for the thermal springs of Laguna Pastos Grandes are between 1.24 and 1.47 whereas the values used by Sanjuan et al. (2014) for their calibrations are never lower than 2.00. Consequently, our data are not in the range of calibration of the equations and if the correlations cannot be extended linearly, the uncertainties on the calculated temperatures will be high.

The geothermometer based on Li isotopes was also tested as it is independent from the Li concentration. This geothermometer was calibrated experimentally on springs from the Guadeloupe and Martinique volcanic arcs (Millot et al., 2010). It relies on the fact that Li isotopic fractionation ($\Delta_{solution\text{-}solid}$) between solution and basalt is strongly temperature dependent with, for example, values of +19.4‰ at 25 °C to 6.7‰ at 250 °C. Considering the δ^7Li mean value of 4.44 ±0.90‰ for thermal springs and using the values for rhyolitic ignimbrite, dacite and andesite in the area that are reported in Table 4, we obtained a fractionation $\Delta_{solution\text{-}solid}$ of 8, 10 and 12‰, respectively. This fractionation is low and can be related to hot temperatures (> 125 °C). Knowing that the Central Andes Ignimbrites are a 50:50 mixture of mantle-derived basalts and of regional crust (de Silva and Kay, 2018), we can hypothesize that the behavior of Li in these rocks and in the altered products is not very different from that in the andesite of Guadeloupe. In this case, the calibration temperature of Millot et al. (2010) would give a temperature of 200 ±25 °C. The Na-K geothermometer yields similar estimates of 228 ±9 °C with the equation of Verma and Santoyo (1997) and 205 ±12 °C with that of Santoyo and Diaz-Gonzalez (2010).

In summary, the geothermometers used in this study yield equilibrium temperatures of spring water with the rocks of a deep reservoir between 150 and 325 °C. The first value (given by silica geothermometer) is too low and reflects a probable precipitation of silica during thermal water cooling. The highest value (given by Na/Li geothermometers) is uncertain because Li concentrations in the fluids are too high for the available calibrations. We thus retain the range of temperature obtained using δ^7Li and Na/K geothermometers, i.e., between 200 and 250 °C, as the maximum temperature encountered by the infiltrated water through the faults of the Pastos Grandes caldera. This temperature is compatible with a depth of 3 km, which corresponds to the top of an ancient pre-eruptive magma reservoir of the volcano (de Silva and Kay, 2018).

4.5 Chemical composition of the water

As extensively demonstrated in previous papers (Stallard and Edmond, 1981; Roche et al., 1991; Moquet et al., 2011), we assumed the atmospheric contribution to groundwater chemistry as negligible in this region and did not correct the data from this contribution. Our results of elemental concentrations obtained in Laguna Pastos Grandes are represented and interpreted together with those from previous studies of this laguna (Ballivian and Risacher, 1981; Hurlbert and Chang, 1984; Risacher and Fritz, 1991; Jones and Renaut, 1994). Spring waters are saline with an average salinity of ~14 g/L compared with the streams with 0.09 g/L of maximum salinity and show homogeneous δ^{37}Cl values of 0.25±0.03‰ (n=12; Table A3). The Piedmont spring is the only exception with a relatively low salinity of 1.9 g/L. The brines from the southeastern part of the laguna are more saline than the water sources (256 g/L; Table 2).

Most of the waters show charge balances better than ±8 % (Table 2), which denote a negligible influence of potential organic charges to the ionic balance. One sample of stream water shows a charge balance of -26% corresponding to an anion excess of 0.41 mM.

The Schoeller diagram (Fig. 5a) shows that streams and springs have different compositions. Sodium and chloride are the dominant ions in spring waters, with average concentrations of 173 and 203 mM, respectively. With a Ca:Mg molar ratio ranging from 1.9 to 2.4, they are all Ca dominant relative to Mg. Hydrothermal springs show similar relative ion concentrations suggesting that a common origin and common processes constrained the chemistry of their major elements (Fig. 5a). Their Ca:alkalinity molar ratio is favorable to the precipitation of calcite (with a ratio of almost one Ca for two C). Compared with the hydrothermal springs, the Piedmont spring is diluted by surface waters. As for the laguna brine, it presents relative ion concentrations similar to those of the hydrothermal springs but with lower alkalinity. Its Ca:alkalinity ratio is not favorable to the precipitation of calcite (Fig. 5b).

4.6 δ^7Li, δ^{11}B and ^{87}Sr/^{86}Sr in waters compared with surrounding rocks

Table 4. Summary of chemical and isotopic data available for dacites, andesites and ignimbrites from Laguna Pastos Grandes. Data in italic are from previous studies cited in parentheses.

Rock type	Ca/Na	Mg/Na	Li (ppm) ±0.3 1SD	δ^7Li (‰)	B (ppm) ±0.3 1SD	δ^{11}B (‰)	Sr (ppm) ±3 1SD	$^{87}Sr/^{86}Sr$
Ignimbrite	0.61	0.30	66.9	-3.33±0.47	54	-7.79±0.21	330	0.725764
Dacite 1	0.70	0.45	147.4	-5.82±0.12	60	-14.88±0.21	351	0.707906
Dacite 2	0.87	0.36	80.2	-5.43±0.35	30	-13.70±0.15	464	0.706951
Andesite 1	1.69	1.50	279.7	-5.11±0.38	144	-13.57±0.09	690	0.705835
Andesite 2	2.13	1.61	147.8	-9.22±0.15	116	-13.89±0.10	706	0.706206
Ignimbrite (Kaiser, 2014)								*0.708173*
Ignimbrite (Kaiser, 2014)								*0.708040*
Cenomanian-Turonian carbonates (McArthur et al., 1994)								*0.707298-0.707428*
Modern marine evaporites (Pierret et al., 2001)								*0.708940*

Thermal springs show homogeneous $^{87}Sr/^{86}Sr$ values slightly more radiogenic than cold streams with average values of 0.70839±0.00002 and 0.70780±0.00021, respectively. In the eastern part of the laguna, the perennial lake has an $^{87}Sr/^{86}Sr$ value of 0.70833, which is slightly lower than thermal spring water values. As expected, all waters are within the range reported for dacites (0.70890±0.00238; Cortecci et al., 2005) and andesites (0.70763±0.00161; Cortecci et al., 2005) of the Andean Central Volcanic Zone. Our dataset is also compared with andesites, dacites and rhyolitic ignimbrites sampled in the vicinity of Laguna Pastos Grandes (Table 4). Sr isotope ratios of streams are between those of Pastos Grandes ignimbrites and dacites, whereas springs and brines show compositions similar to ignimbrites (Fig. 6a). The $^{87}Sr/^{86}Sr$ value of Cenomanian-Turonian marine carbonates, considered as the last open marine period in the central Andes (Deconinck et al., 2000), is much lower than the values of the thermal springs (with $^{87}Sr/^{86}Sr$ = 0.7073-0.7074; McArthur et al., 1994).

Similarly, the boron and lithium isotopic compositions of collected waters are clearly different from seawater composition (δ^{11}B = 39.6‰ and δ^7Li = 31.0‰; Boschetti et al., 2017). δ^{11}B and δ^7Li values increase between rock and water samples in the following order: volcanic rocks < hydrothermal springs = lake brines < surface runoff. Pastos Grandes' thermal waters and brine show homogeneous δ^{11}B and δ^7Li values around -5.5 and +4.1 ‰, respectively (Fig. 6b). In comparison, one stream displays more positive values for both δ^{11}B and δ^7Li, at 0 and 10.9‰, respectively, whereas surrounding volcanic rocks are more negative, with δ^{11}B between -14.9 and -7.8‰ and δ^7Li between -9.2 and -3.3‰ (Fig. 6b; Table 4). In the studied area, volcanic rocks have high Li and B concentrations (67–280 ppm of Li and 30–144 ppm of B) and isotopic compositions depleted in ^{7}Li and ^{11}B compared with the range of values for the Andean volcanic arc: 3-9 ppm of Li with -6.4 < δ^7Li < -4.5‰ (Chan et al., 2002) and 6-60 ppm of B with -7 < δ^{11}B

562 < +4‰ (Rosner et al., 2003). Our boron isotopic compositions are similar to the continental
563 crust ($\delta^{11}B$ usually between -15 and -10‰; Chaussidon and Albarède, 1992).

564 ### 4.7 Thermodynamic model

565 We compared the average spring water composition and the water chemistry obtained
566 using PHREEQC modeling of the alteration of the volcanic bedrock at 200-250 °C with a
567 CO_2 partial pressure between 10 and 100 bar (typical of CO_2-rich geothermal systems;
568 Lowenstern, 2001). The objective was to determine if the observed concentrations of major
569 cations (Ca, Mg, K, Na and Si) can be reached by dissolution of the volcanic rocks (Table
570 A4, see Appendix for the PHREEQC model) without input of ancient marine sediments.
571 For the bedrock's mineral composition, we selected from the minerals available in the
572 Thermoddem database those closer to the mineralogy observed in the volcanic rocks
573 surrounding Laguna Pastos Grandes (details in Appendix):
574 – Albite for the source of Na
575 – Anorthite for Ca
576 – Pargasite for Mg
577 – Quartz for Si
578 – Sanidine for K
579 In all the models tested, Si concentration and DIC are higher than in the spring water. For
580 Ca, Mg, K and Na concentrations, the best result is obtained at 225 °C with 20 bar of CO_2
581 (SI=1.3; Fig. 7). To adjust the Cl concentration in the water, we tried different Cl sources:
582 pure magmatic $Cl_2(g)$ or halite. The modeling results were not conclusive with pure
583 magmatic $Cl_2(g)$ but consistent with halite, suggesting that the salinity of the spring water
584 is provided by the dissolution of halite. Because halite is commonly associated with
585 gypsum in the sedimentary record of the Andean region, we also added anhydrite to the
586 bedrock composition in the model. Despite this, the main Ca source in the spring waters
587 remains the anorthite (Table A4). All the minerals were considered in the calculation as
588 infinite reservoirs except for halite, which was fixed by the average Cl concentration in the
589 spring water (239 mM).

590 ## 5. Discussion

591 *Table 5. Comparison of Laguna Pastos Grandes characteristics with Chilean and Bolivian*
592 *salars. Data from this study and Hoke et al., 1994; Spiro et al., 1997; Risacher et al., 2003,*
593 *2011; Risacher and Fritz, 1991, 2009. ul: ulexite; hal: halite; gyps: gypsum; mirab:*
594 *mirabilite. *Previous data TDS: Total Dissolved Solids*

	Laguna Pastos Grandes	**Chilean salars**	**Bolivian salars**
Location	Bolivian Altiplano	Western Cordillera	Bolivian Altiplano
Basement	Dacite-Andesite-Rhyolitic Ignimbrite	Rhyolitic ignimbrite Andesite	Andesite Rhyodacite
Altitude	4450 m	3400-4300 m	4100-4600 m
Surface	130 km^2	0.03-400 km^2	0.03-500 km^2
Potential evaporation	1400 mm/year	1000-2000 mm/year	1000-1500 mm/year
Precipitation	100 mm/year	40-380 mm/year	50-150 mm/year
Mean temperature	5 °C	0 °C	5-10 °C
Morphology	Playa lake	Mainly playa lakes	Mainly playa lakes
Salinity	256 g/l	1.2-365 g/l	0.4-348 g/l
Brine type *(Na-Cl-)*	Ca	65% $_{SO4}$ – 24% $_{Ca}$	52% $_{SO4}$ – 26% $_{CO3}$ – 19% $_{Ca}$
Salts	Calcite-gyps.-ul.-hal.	Gyps.-hal.-mirab.-ul.	Gyps.-hal.-mirab.-ul.
Infiltration rate	~negligible	0.01-12.8% of outflow	0.01% - ~inflows

Thermal influence *(T>15°C)*	Yes	78 %	60%
Spring T_{max}	47 °C (20-75 °C*)	83 °C (Puchuldiza)	36 °C (Challviri)
Spring TDS (range)	14 g/l	3.8 g/l in average (0.2-21.8)	0.82 g/l in average (max. 14)
Mantle influence	47%	69%	44%
CO_2 isotopic composition	-11‰	-8 to -0.6‰	-20 to -6‰

Laguna Pastos Grandes is a calcic-type salar characterized by Na-Ca-Cl brines which can, according to thermodynamic models, lead to the precipitation of calcite, the first mineral of the evaporative pathway before gypsum and ulexite (Hardie and Eugster, 1970; Risacher and Fritz, 2009). Despite the fact that the calcic-type salar represents 19% of the salars in Bolivia (n=6) and 24% in Chile (n=12, Table 5), modern massive calcite precipitations are only observed in Laguna Pastos Grandes whereas gypsum, mirabilite (Na_2SO_4), halite and ulexite dominate other calcic salars. For example, Laguna Capina in Bolivia shows similar water chemistry and mineralogical characteristics to Laguna Pastos Grandes with the exception of its massive calcite precipitation (Ballivian and Risacher, 1981). This means that at least one other parameter than the Ca^{2+} concentration varies between the Andean salars and controls the extent of calcite precipitation in Laguna Pastos Grandes. Despite the fact that carbonate mineral precipitation is tremendously complicated by biomineralization processes (mainly associated here with micro-organisms; Jones and Renaut, 1994) and reaction kinetics in a non-ideal near-surface continental environment (with ion interactions, variable substrates, fluctuating pH, organic molecules and gas phase interactions; Alonso-Zarza and Tanner, 2010), we can consider that the fundamental reason for calcite to precipitate in significant amounts is because both $Ca^{2+}_{(aq)}$ and $CO_3^{2-}{}_{(aq)}$ are supplied in sufficient concentrations by water inflows to dynamically sustain the supersaturation relative to calcite. The focus of our investigations is therefore on the origin of the CO_2 and Ca enrichments in water inflows.

5.1 Origin of CO_2 and N_2 in thermal spring gases

The thermal springs of Laguna Pastos Grandes discharge not only thermal waters but also gases that are essentially mixtures of CO_2 and N_2 (Table 1) like the other gas sources identified in the Central Andes (Spiro et al., 1997). Changes in the relative proportions of CO_2 and N_2 gas between sources in Laguna Pastos Grandes can be partly attributed to changes in the contribution from Air Saturated Waters (ASW) to the hydrothermal system feeding the carbonate platform. Indeed, the $^{40}Ar/^{36}Ar$ mean value of 289.3 is close to the air value of 295.5 (Nier, 1950). The air-normalized abundances of the Atmosphere-Derived Noble Gases (ADNG: ^{20}Ne and ^{36}Ar) for all samples show a degree of depletion correlated with elemental mass of the noble gases (Ne > Ar), which is consistent with the water-solubility fractionation of air (Fig. 3). The atmospheric component found in thermal springs (including O_2 and the atmospheric proportion of N_2) is therefore related to an ASW component and not the result of air-contamination during sampling.

Despite this ASW component, the average R_C/R_A value of 3.79 ± 0.08 (Fig. 3, Table 1) indicates the presence of mantle-derived helium in the ascending hydrothermal flux. Our helium isotope results supplement and confirm previous data on the Central Andes including one isolated analysis in Laguna Pastos Grandes (Fig. A2; Hilton et al., 1993; Hoke et al., 1994). Assuming that pure mantle-derived helium is characterized by R_C/R_A ~8, we deduced that ~47 % of the helium at Laguna Pastos Grandes is of mantle origin (using calculations described in Hoke et al., 1994; Table 1) whereas it does not exceed 20%

636 in other gas sources from the Altiplano. In the Western Cordillera, however, the mantle
637 helium contribution rises up to 69% at the Isluga volcano in Chile, 300 km north of Laguna
638 Pastos Grandes close to the Chilean-Bolivian border (Hoke et al., 1994). Therefore, the
639 particularly high mantle influence in Laguna Pastos Grandes compared with that of the
640 Bolivian Altiplano is probably due to its proximity to the active volcanic arc of the Western
641 Cordillera (Table 5; Springer and Förster, 1998). This is consistent with the fact that the
642 Laguna Pastos Grandes' thermal springs also show the highest temperature recorded in
643 salar springs in the Altiplano with a maximum temperature observed by Jones and Renaut
644 (1994) of 75 °C and 46 °C in this study (Table 5). For comparison purposes, the maximum
645 temperature recorded in the Western Cordillera is about 87 °C (Puchuldiza salar, northern
646 Chile; Risacher et al., 2011).
647
648 Yet, the average $\delta^{13}C$ value of CO_2 ~ -11.1 ± 0.1‰ is lower than the typical value of a
649 magmatic mantle-derived CO_2 source (between -9 and -4‰; Hoefs, 1980). Two hypotheses
650 can be proposed to explain this low value: a contribution of CO_2 from sedimentary sources,
651 i.e., organic carbon with $\delta^{13}C$ < -20‰ (Hoefs, 1980) or carbonate precipitation during fluid
652 ascent. To trace the origin of the CO_2, $\delta^{13}C$ values of the gas samples are typically
653 interpreted in relation to $CO_2/^3He$ values (Sano and Marty, 1995). However, in Laguna
654 Pastos Grandes, hydrothermal degassing and liquid-vapor partitioning could have
655 significantly affected the $\delta^{13}C$ and $CO_2/^3He$ values of the gas. We thus determined the
656 $CO_2/^3He$ composition at threshold P-T degassing conditions using calculations of fluid
657 phase equilibria applied to our system (H_2O-NaCl-CO_2-N_2-O_2-He-Ne-Ar; Rouchon et al.,
658 2016). We assumed that all the gaseous CO_2 had been exsolved at a single depth of
659 supersaturation and that there were no carbonate precipitation effects on the $CO_2/^3He$ value
660 considering the acid pH ~6 of hydrothermal fluids. The best results were obtained with an
661 initial meteoric water recharge at high altitude, i.e., 5500 m, and with a temperature of 0
662 °C. This is consistent with the $\delta^{18}O$ and $\delta^{2}H$ relationship in the spring waters, which
663 suggests that the geothermal reservoir is fed during the wet season by meteoric water of
664 rainfall isotopic composition (i.e., $\delta^{18}O$ of -16‰ and $\delta^{2}H$ of -123‰; Fig. 4 and Table A2
665 for values). Snow deposited during the dry season shows completely different isotopic
666 compositions (minimum $\delta^{18}O$ of -6.8‰ and $\delta^{2}H$ of -30.3‰). Considering a local geotherm
667 of 45 °C/km (Rothstein and Manning, 2003), we obtained between 17 and 49% of CO_2
668 exsolution at a degassing depth of approximately 25-35 m (at 2.5-3.5 bar) in the different
669 springs (Table 1). Before degassing, the $CO_2/^3He$ values were consequently higher than
670 those measured at the surface and between $4.7*10^8$ and $2.9*10^9$. These values are within
671 the range or slightly lower than the mantle value of $2*10^9$ (Marty and Jambon, 1987). This
672 depletion of CO_2 relative to ^3He in the fluids compared with the mantle value could be fully
673 compatible with carbonate precipitation during the geothermal fluid ascent. Given that
674 carbonates are enriched in ^{13}C compared with CO_2, this would also explain why the
675 remaining CO_2 in the gas is depleted on ^{13}C. We cannot, however, completely rule out a
676 minor contribution from the organic matter of underlying but unknown sedimentary rocks
677 possibly accompanied to some extent by carbonates, which could account for the small
678 shift towards negative $\delta^{13}C_{CO2}$ values compared with the mantle.
679
680 Likewise, the $\delta^{15}N$ values between 2.3 and 6.4‰ could reflect a sedimentary (+10‰ >
681 $\delta^{15}N$ > -5‰; e.g. Ader et al. 2016) or crustal (mean $\delta^{15}N$ = +7‰; e.g. Sano et al., 1998)
682 contribution mainly generated by organically sourced nitrogen sequestered in sedimentary
683 rocks through biologic activity and sedimentation (Boyd, 2001). Although stratovolcanoes

and their products dominate the South Lipez landscape of the Altiplano (Avila-Salinas, 1991; de Silva and Francis, 1991; Richter et al., 1992), the volcanic rocks have likely overlain (Ludington et al., 1975) or incorporated (Risacher and Alonso, 2001) Cretaceous and Early Tertiary clastic to evaporitic sediments. In particular, the Cretaceous El Molino Formation is known to contain several organic-rich units with TOC up to 4.2% (Camoin et al., 1991; Blanc-Valleron et al., 1994). Unfortunately, it remains unclear whether the El Molino Formation extends in the South Lipez region. Alternatively, this region being close to the subduction zone of the Nazca plate below the South American plate (with the slab located at a depth of ~150-km below the Altiplano; Hoke et al., 1994; Kay and Coira, 2009), organic carbon and nitrogen may be remobilized from the slab by metamorphism (Gorman et al., 2006) and transported through primary melts into crustal intrusions. This hypothesis is supported by the high concentrations of Li associated with light δ^7Li recorded in volcanic lava flows surrounding Laguna Pastos Grandes (compared with MORB composition representing the upper mantle, δ^7Li = 3.7‰ Misra et al., 2012), which can only be interpreted as the addition of highly-negative δ^7Li slab-derived fluids component to the mantle wedge beneath our studied area (Fig. 8; Chan et al., 2002). Boron is also highly concentrated in the volcanic rocks of the area (30-144 ppm) and could derive from the same source as the Li. However, δ^{11}B values, between -14 and -8‰ are more negative than the lowest value of the slab-derived fluids predicted for the Andes (> -2.8‰; Rosner et al., 2003). B is more volatile than Li and light δ^{11}B values are commonly observed in magmatic rocks (Chaussidon and Albarède, 1992) due to magma degassing effects, which produce ^{11}B depletion in the residual melt (Jiang and Palmer, 1998).

5.2 Hydrological history of spring water

The question of the origin of spring waters in Andean salars has been examined in previous studies (Risacher and Fritz, 1991; Risacher et al., 2003; Risacher and Fritz, 2009). Risacher et al. (2003) proposed that saline lakes are continuously leaking through their bottom sediments, feeding most of the dissolved components to groundwater. In this case, the relative rate of infiltration and meteoric water recharge would control the lake's salinity and the concentration of conservative components in the system (Sanford and Wood, 1991). We thus used the isotopic composition of the water to determine the origin (and the evolution) of the spring waters in Laguna Pastos Grandes. Spring waters lie on the local Ground and Spring Water Line (LGSWL) with slightly more positive δ^{18}O and δ^2H values than rainfall, implying evaporative enrichment in both ^{18}O and ^{2}H of the meteoric water prior to infiltration at high altitude (Fig. 4b; Bershaw et al., 2016). Another explanation for this enrichment could be the loss of vapor during the ascent of thermal fluids from the reservoir to the surface (Cortecci et al., 2005). The hydrothermal springs are thus genetically linked to the meteoric waters. The Piedmont thermal source, which is the coldest spring (32 °C), less saline than others, and located on the border of the laguna, shows more negative δ^{18}O and δ^2H values, suggesting a dilution of thermal spring water by meteoric water (Fig. 4). By comparison, the brine of the laguna is very enriched in ^{18}O and ^{2}H, ruling out the hypothesis of an important recharge of the springs by infiltration of the laguna brine. The Cl/Br values of spring waters are also not consistent with a dilution of recycled brines by mixing with groundwater or meteoric water (Fig. 5c). It suggests that the chemistry of the spring waters more likely derives from the alteration of the bedrock minerals.

5.3 Volcanic bedrock alteration at high temperature and pCO_2

δ^7Li and Na/K geothermometers applied to spring waters indicate that the meteoric water reached a maximum temperature of 200-250 °C after infiltration. Due to the high mantle-derived CO_2 flux delivered in thermal springs, the estimated pCO_2 in these waters (between 3 and 389 mbar estimated by PHREEQC; Table 2) spans the range and even exceeds the pCO_2 in spring waters from both the Altiplano and the Western Cordillera with 40 – 120, and 10 – 340 mbar, respectively (Morteani et al., 2014). This CO_2 enrichment can acidify thermal waters to a pH ~5 and give groundwater the ability to dissolve the bedrock minerals and acquire a large enrichment in solute load and especially in Ca. To test this hypothesis, we performed a series of PHREEQC modeling to determine the water composition resulting from the alteration of the volcanic bedrock with possible evaporites (halite, gypsum and anhydrite) from a meteoric water at 200, 225 and 250 °C with different CO_2 partial pressures and compared the results with the average spring water composition (Table A4; Fig. 7).

The best results for Ca, Mg and K concentrations in spring waters were obtained by the alteration of volcanic minerals at a temperature of 225 °C, which is the average temperature determined using geothermometers, and 20 bar of CO_2 (Fig. 7). This amount of CO_2 is compatible with the proximity of an ancient pre-eruptive magma reservoir of the volcano at a depth of ~3 km as suggested by de Silva and Kay (2018). Under these conditions, the main source of Ca in the water is the dissolution of Ca-rich felspars rather than anhydrite (Table A4). These results are corroborated by Sr isotope data, which suggest that local meteoric waters interact with the host volcanic rocks (dacite, andesite and rhyolitic ignimbrite) rather than with ancient marine carbonates (Fig. 6a). Similarly, thermal waters and the laguna brine show δ^7Li and $\delta^{11}B$ values not far from those of the surrounding volcanic rocks (Fig. 6b). δ^7Li values measured in waters are on average 8‰ higher than those measured in the surrounding rocks. This shift has been commonly observed in hydrothermal systems (e.g., von Strandmann et al., 2006; Godfrey et al., 2013) and experimental works showed that the difference between the δ^7Li values of the water and weathered volcanic rocks must be due to equilibrium isotopic fractionation at high temperature (Δ^7Li between 9.5‰ at 200 °C and 6.7‰ at 250 °C; Millot et al., 2010). The average 7‰ positive $\delta^{11}B$ shift between springs and volcanic rocks can be explained either by adsorption of B on mineral surfaces during the ascent and cooling of hydrothermal fluid to the spring vent or by the preferential incorporation of light B during carbonate precipitation.

The water chemistry obtained with these simulations is over-saturated with different carbonate minerals ($SI_{calcite}$=1.23, $SI_{dolomite}$=3.03, $SI_{magnesite}$=2.02), which supports the hypothesis deduced from $CO_2/^3He$ and $\delta^{13}C$ data that carbonate could have precipitated during fluid ascent. The higher Si concentration obtained in our simulations compared with those measured in spring waters together with the low temperature given by the SiO_2 geothermometer also indicate precipitation of silica during fluid ascent. The simulations suggest, however, that the salinity of the spring water is most probably delivered by the dissolution of halite deposits. This interpretation is confirmed by the homogeneous $\delta^{37}Cl$ values of the springs of 0.25±0.03‰ on average (n=12; Table A3), which are close to the $\delta^{37}Cl$ value expected for the precipitation of halite in equilibrium with seawater at 0‰ and 25 °C ($\delta^{37}Cl$ = 0.30‰; Eggenkamp et al., 1995, 2016). It indicates that over time, multiple cycles of precipitation and dissolution of halite without new inputs of Cl to the laguna have

779 homogenized the Cl isotopic composition of the laguna brine and salts. Therefore, we can
780 assume that Na and Cl derive from ancient marine halite deposits, which could have formed
781 during the last Cenomanian-Turonian marine period. In the studied area, these deposits,
782 which have been remobilized in the continental overlying Cretaceous and Tertiary deposits
783 (Deconinck et al., 2000), could have been either overlain by volcanic rocks or incorporated
784 by volcanic eruptions as suggested by Risacher and Alonso (2001) for gypsum. This is also
785 consistent with Cl and Na concentrations in these waters, which display a covariant trend
786 close to equimolarity, typical of halite leaching (Fig. A3).
787
788 **5.4 How is Laguna Pastos Grandes unique?**
789
790 Ca:alkalinity molar ratios of the different waters of Laguna Pastos Grandes show that only
791 the thermal springs have the potential to precipitate calcite (Fig. 5b). Stream waters and
792 mixed sources (Piedmont) are too diluted to contribute to the growth of the carbonate
793 platform, and the laguna brine, which derives from the spring waters (as suggested by Sr,
794 chemical and isotopic data; Figs. 4, 5, 6) has been depleted in carbonate relative to Ca.
795 Most of the salars in the Central Andes are fed by thermal spring inflows (60% in Bolivia
796 and 78% in Chile) enriched in solutes compared with streams and regional groundwater
797 (Table 5; Risacher and Fritz, 1991; Risacher et al., 2011). However, modern carbonate is
798 absent or minor in these systems and generally precipitated as the first mineral of a more
799 developed evaporitic sequence (Risacher and Fritz, 2009). Laguna Pastos Grandes is
800 unique in this respect, as it displays a ~40 km^2 recent-to-modern carbonate platform
801 spatially associated with thermal waters. These waters not only show a remarkable mantle
802 influence on temperature and gas composition but also one of the highest enrichments in
803 solutes of the Central Andes with an average salinity of 14 g/l (Fig. 8; Table 5). This could
804 be indicative of the significant alteration rate of the hydrothermal system of Laguna Pastos
805 Grandes compared with the other salars due to the high flow of CO_2 gas from the mantle.
806 Moreover, the singularity of this laguna is also likely related to a particular mineralogy of
807 the volcanic bedrock since calcic-type salars are limited in the Andean region. For example,
808 Chilean volcanic rocks are known to be particularly enriched in sulfides (Risacher and
809 Alonso, 2001) and could be responsible for the genesis of a majority of sulfate-type salars
810 (65%) rather than calcic-type salars.

811 **6. Conclusion and perspectives**

812 To the first order, Bolivian and Chilean salars belong to the same climatic, geologic and
813 hydrologic environment (Risacher and Fritz, 2009). Nevertheless, they present a great
814 diversity of chemistry and salt types, which result from local variations in fluid sources and
815 climate parameters. We have shown in this study that the western part of Laguna Pastos
816 Grandes, characterized by abundant recent-to-modern carbonate deposits, is mainly fed by
817 thermal spring water with minor contributions of rainfall and surrounding streams, all of
818 meteoric origin. These spring waters show $Ca^{2+}_{(aq)}$ and CO_3^{2-} in sufficient concentrations
819 to be over-saturated with calcite. Both solutes can originate from the alteration of the
820 volcanic bedrock by highly CO_2-enriched fluids heated at ~225 °C. The magmatic mantle-
821 derived CO_2 and the particularly high heat flow that drive the fluid circulation to the surface
822 are probably due to a shallow pre-eruptive magma chamber as suggested by de Silva et al.
823 (2006) and de Silva and Kay (2018) (i.e., at a typical depth of ~5 km; Fig. 8). This
824 configuration thus fulfills all the essential criteria to provide solutes and precipitate large
825 volumes of carbonates in comparison with most other modern Andean salars.

This configuration is not exclusive to the Andean geodynamic system and can be found in many continental extensional settings (e.g., in Afar) where we posit, by analogy, that the same mechanisms act as key factors in the genesis of continental carbonate deposits in pure volcanic provinces. The main components of this favorable configuration would be, as identified in this study, a deep source of CO_2 and the Ca-rich volcanic basement allowing the following processes to occur:

i. Alteration of a sulfide-poor volcanic bedrock containing Ca-enriched minerals (usually feldspars) at high pCO_2 and high temperature, leading to cationic enrichment of the waters and producing calcic type hydrothermal waters.

ii. When the hydrothermal waters emerge at the surface as springs and encounter the much lower atmospheric levels of pCO_2, CO_2 is massively degassed leading to a pH increase. These concomitant processes drive the solution to precipitate carbonates. CO_2 loss may also be driven by photosynthesis.

iii. High evaporation rates at the surface, increasing the solute concentrations above calcite saturation.

Laguna Pastos Grandes is, therefore, a unique natural laboratory that shows a great diversity of carbonate facies (including pisoliths, ooids, muds and microbialites; Risacher and Eugster, 1979; Jones and Renaut, 1994; Bougeault et al., 2019), some of them remarkably similar to ancient equivalents such as Cretaceous Presalt carbonates (Terra et al., 2010; Tosca and Wright, 2015; Muniz and Bosence, 2015). This laguna could, therefore, be further used to trace the biotic and/or abiotic controls at play in the formation of these carbonate deposits. Indeed, microbial mats and thin, dark, mucilaginous films locally coating the pool floors and pisolith surfaces in Laguna Pastos Grandes (described by Jones and Renaut, 1994 and Bougeault et al., 2019) might also contribute to the carbonate precipitation (Pace et al., 2018; Gomez et al., 2018). Comprehensive geochemical, mineralogical and biodiversity studies are underway on the whole carbonate platform of Pastos Grandes to characterize the link between physicochemical parameters, microbial communities and the diversity of carbonate fabrics observed. These results will provide clues to identify the biosignatures in modern microbialites and enable us to further interpret the sedimentary record on our planet and beyond.

Acknowledgments, Samples, and Data

We would like to thank Total E&P Bolivia for field assistance (Serge Nicoletis, Jean-Pierre Meunier, Olivier-Daniel Moreau, Rozmarie Cuellar) and Total Lab (CSTJF, Pau, France; Carole Bortelle, Josiane Sentenac, Valérie Burg) for water analysis; Mathilde Mercuzot (Univ. Burgundy) for field and laboratory assistance (2016); Antoine Cogez for strontium isotopic analysis of volcanic rocks, Pierre Burckel for the chemical composition analysis of volcanic rocks, and BRGM (Catherine Guerrot team) for the chemical and isotopic measurements in water samples (2016). We would also like to thank Dr. Daniel Carrizo for providing the Chilean geological map. Particular thanks go to Magali Bonifacie for the constructive discussion on chlorine isotope data. Funding was provided by Total EP R&D Carbonate Project (E. Poli). Parts of this work were supported by IPGP's multidisciplinary program PARI, and by the Paris–IdF region SESAME Grant no. 12015908.
This is IPGP contribution No. 4062.

References

Ader M., Thomazo C., Sansjofre P., Busigny V., Papineau D., Laffont R., ... and Halverson G. P. (2016) Interpretation of the nitrogen isotopic composition of Precambrian sedimentary rocks: Assumptions and perspectives. *Chemical Geology* **429**, 93-110.

Ahlfeld F. (1956) Sodaseen in Lipez (Bolivien). *Neues Jb. Miner. Mh.* **6/7**, 128-136.

Ahlfeld F. and Branisa L. (1960) Geologia de Bolivia: Instituto Boliviano del Petróleo, Ed. Dom Bosco, La Paz.

Alonso-Zarza A. M. and Tanner L. H. (2010) Carbonates in continental settings: Facies, environments, and processes: Developments in Sedimentology **61**, pp. 378.

Assayag N., Jézéquel D., Ader M., Viollier E., Michard G., Prévot F., and Agrinier P. (2008) Hydrological budget, carbon sources and biogeochemical processes in Lac Pavin (France): constraints from $\delta^{18}O$ of water and $\delta^{13}C$ of dissolved inorganic carbon. *Applied Geochemistry* **23**(10), 2800-2816.

Avila-Salinas S. (1991) Petrologic and tectonic evolution of the Cenozoic volcanism in the Bolivian western Andes. In *Andean Magmatism And Its Tectonic Setting* (eds. R.S. Harmon and C.W. Rapela). Spec. Pap. geol. Soc. Am. **265**, 245-257.

Ballivian O. and Risacher F. (1981) Los salares del altiplano boliviano: métodos de estudio y estimación económica. IRD Editions.

Bershaw J., Saylor J.E., Garzione C.N., Leier A. and Sundell K.E. (2016) Stable isotope variations ($\delta^{18}O$ and $\delta^{2}H$) in modern waters across the Andean Plateau. *Geochimica et Cosmochimica Acta* **194**, 310–324.

Blanc P., Lassin A., Piantone P., Azaroual M., Jacquemet N., Fabbri A., and Gaucher E.C. (2012) Thermoddem: A geochemical database focused on low temperature water/rock interactions and waste materials. *Applied Geochemistry* **27(10),** 2107-2116.

Blanc-Valleron M.-M., Schuler M., Rauscher R., Camoin G. and Rouchy J.-M. (1994) La matière organique des séries d'âge Crétacé supérieur-Tertiaire inférieur du bassin de Potosi (Cordillère orientale, Bolivie): apports stratigraphiques et paléo-géographiques. *C.R. Acad. Sci. Paris II* **319**, 1359-1366.

Bonifacie M., Charlou J. L., Jendrzejewski N., Agrinier P. and Donval J. P. (2005) Chlorine isotopic compositions of high temperature hydrothermal vent fluids over ridge axes. *Chemical Geology* **221**(3-4), 279-288.

Boschetti T., Cortecci G., Barbieri M. and Mussi M. (2007) New and past geochemical data on fresh to brine waters of the Salar de Atacama and Andean Altiplano, northern Chile. *Geofluids* **7**(1), 33-50.

Boschetti T., Toscani L., Iacumin P. and Selmo E. (2017) Oxygen, Hydrogen, Boron and Lithium Isotope Data of a Natural Spring Water with an Extreme Composition: A Fluid from the Dehydrating Slab? *Aquatic Geochemistry* **23**(5-6), 299-313.

Boyd, S. R. (2001). Nitrogen in future biosphere studies. *Chemical Geology* **176**(1-4), 1-30.

Camoin G., Rouchy J.M., Babinot J.F. Deconinck J.F. and Tronchetti G. (1991) Dynamique sédimentaire et évolution paléogéographique d'un bassin continental en position d'arrière-arc: le Maastrichtien de la Cordillère orientale (Bolivie). *C.R. Acad. Sci. Paris II* **312**, 1335-1341.

Chaffaut I., Coudrain-Ribstein A., Michelot J. L. and Pouyaud B. (1998) Précipitations d'altitude du Nord-Chili, origine des sources de vapeur et données isotopiques. *Bull. Inst. Fr. Etudes andines* **27**, 367-384 (in French).

Chan L.H., Edmond J.M., Thompson G. and Gillis K. (1992) Lithium isotopic composition of submarine basalts: implications for the lithium cycle in the oceans. *Earth Planet. Sci. Lett*. **108**, 151–160.
Chan L.H. and Kastner, M. (2000) Lithium isotopic composition of pore fluids and sediments in the Costa Rica subduction zone: implications for fluid processes and sediment contribution to arc volcanoes. *Earth Planet. Sci. Lett.* **183**, 275–290.
Chan L. H., Leeman W. P. and You C. F. (2002) Lithium isotopic composition of Central American volcanic arc lavas: implications for modification of subarc mantle by slab-derived fluids: correction. *Chemical Geology* **182**(2-4), 293-300.
Chaussidon M. and Marty B. (1995) Primitive boron isotope composition of the mantle. *Science* **269**, 383–386.
Chetelat B., Liu C.-Q., Gaillardet J., Wang Q.L., Zhao Z.Q., Liang C.S., Xiao Y.K. (2009) Boron isotopes geochemistry of the Changjiang basin rivers. *Geochim. Cosmochim. Acta* **73**, 6084-6097.
Claypool G. E., Holser W. T., Kaplan I. R., Sakai H. and Zak I. (1980) The age curves of sulfur and oxygen isotopes in marine sulfate and their mutual interpretation. *Chemical Geology* **28**, 199-260.
Cortecci G., Boschetti T., Mussi M., Lameli C. H., Mucchino C. and Barbieri M. (2005) New chemical and original isotopic data on waters from El Tatio geothermal field, northern Chile. *Geochemical Journal* **39**(6), 547-571.
Deconinck J. F., Blanc-Valleron M. M., Rouchy J. M., Camoin G. and Badaut-Trauth D. (2000) Palaeoenvironmental and diagenetic control of the mineralogy of Upper Cretaceous–Lower Tertiary deposits of the Central Palaeo–Andean basin of Bolivia (Potosi area). *Sedimentary Geology* **132**(3-4), 263-278.
Dellinger M., Gaillardet J., Bouchez J., Calmels D., Louvat P., Dosseto A., Gorge C., Alanoca L. and Maurice L. (2015) Riverine Li isotope fractionation in the Amazon River basin controlled by the weathering regimes. *Geochimica et Cosmochimica Acta* **164**, 71-93.
de Silva S. L. and Francis P. W. (1991) Volcanoes of the Central Andes. Springer Verlag, Berlin.
de Silva S., Zandt G., Trumbull R., Viramonte J. G., Salas G. and Jimenez N. (2006) Large ignimbrite eruptions and volcano-tectonic depressions in the Central Andes: a thermomechanical perspective. In: Trois, C., De Natale, G., Kilburn, C.R.J. (Eds.), Mechanism of Activity and Unrest at Large Calderas, vol. 269. Geol. Soc. London, Spec. Publ., pp. 47-63.
de Silva S. and Kay S.M. (2018) Turning up the Heat: High-Flux Magmatism in the Central Andes. *Elements* **14**, 245-250.
Durand N., Monger H. C., Canti M. G. and Verrecchia E. P. (2018) Calcium carbonate features. In Interpretation of micromorphological features of soils and regoliths. Elsevier. pp. 205-258.
Eggenkamp H. (1994) δ^{37}Cl: The geochemistry of chlorine isotopes. Faculteit Aardwetenschappen, Universiteit Utrecht. Geologica Ultraiectina, (116).
Eggenkamp H.G.M., Kreulen R., and Koster Van Groos A.F., (1995) Chlorine stable isotope fractionation in evaporites. *Geochim. Cosmochim. Acta* **59** (24), 5169–5175.
Eggenkamp H. G. M., Bonifacie M., Ader M., and Agrinier P. (2016) Experimental determination of stable chlorine and bromine isotope fractionation during precipitation of salt from a saturated solution. *Chemical Geology* **433**, 46-56.

Flesch G. D., Anderson Jr A. R. and Svec H. J. (1973) A secondary isotopic standard for $^{6}Li/^{7}Li$ determinations. *International Journal of Mass Spectrometry and Ion Physics* **12**(3), 265-272.
Fouillac C. and Michard G. (1981) Sodium/lithium ratio in water applied to geothermometry of geothermal reservoirs. *Geothermics* **10**(1), 55-70.
Fournier R. O. and Potter Ii R. W. (1979) Magnesium correction to the Na/K/Ca chemical geothermometer. *Geochimica et Cosmochimica Acta* **43**(9), 1543-1550.
Fritz P., Suzuki O., Silva C. and Salati E. (1981) Isotope hydrology of groundwaters in the Pampa Del Tamarugal, Chile. *Journal of Hydrology* **53**, 161–184.
Gaillardet J. and Allègre C. J. (1995) Boron isotopic compositions of corals: Seawater or diagenesis record? *Earth and Planetary Science Letters* **136**(3-4), 665-676.
Giunta T., Ader M., Bonifacie M., Agrinier P. and Coleman M. (2015a) Pre-concentration of chloride in dilute water-samples for precise $\delta^{37}Cl$ determination using a strong ion-exchange resin: Application to rainwaters. *Chemical Geology* **413**, 86-93.
Godfrey L. V., Chan L. H., Alonso R. N., Lowenstein T. K., McDonough W. F., Houston J., Li J., Bobst A. and Jordan T. E. (2013) The role of climate in the accumulation of lithium-rich brine in the Central Andes. *Applied Geochemistry* **38**, 92-102.
Godon A., Jendrzejewski N., Eggenkamp H. G., Banks D. A., Ader M., Coleman M. L. and Pineau F. (2004) A cross-calibration of chlorine isotopic measurements and suitability of seawater as the international reference material. *Chemical Geology* **207**(1-2), 1-12.
Gomez F. J., Kah L. C., Bartley J. K. and Astini R. A. (2014) Microbialites in a high-altitude Andean lake: multiple controls on carbonate precipitation and lamina accretion. *Palaios* **29**(6), 233-249.
Gomez F. J., Mlewski C., Boidi F. J., Farías M. E. and Gérard E. (2018) Calcium carbonate precipitation in diatom-rich microbial mats: the Laguna Negra hypersaline lake, Catamarca, Argentina. *Journal of Sedimentary Research* **88**(6), 727-742.
Gorman P. J., Kerrick D. M. and Connolly J. A. D. (2006) Modeling open system metamorphic decarbonation of subducting slabs. *Geochemistry, Geophysics, Geosystems* **7**(4).
Hardie L. A. and Eugster H. P. (1970) The evolution of closed-basin brines. *Mineralogical Society of America Special Paper* **3**, 273-290.
Hilton D. R., Hammerschmidt K., Teufel S. and Friedrichsen H. (1993) Helium isotope characteristics of Andean geothermal fluids and lavas. *Earth and Planetary Science Letters* **120**(3-4), 265-282.
Hoefs J. (1980) *Stable isotope geochemistry*. Berlin and Heidelberg, Springer Verlag.
Hoke L., Hilton D. R., Lamb S. H., Hammerschmidt K. and Friedrichsen H. (1994) ^{3}He evidence for a wide zone of active mantle melting beneath the Central Andes. *Earth and Planetary Science Letters* **128**(3-4), 341-355.
Horita J. (2014) Oxygen and carbon isotope fractionation in the system dolomite–water–CO_2 to elevated temperatures. *Geochimica et Cosmochimica Acta* **129**, 111-124.
Hurlbert S. H. and Chang C. C. (1984) Ancient ice islands in salt lakes of the Central Andes. *Science* **224**(4646), 299-302.
Iltis A., Risacher F. and Servant-Vildary S. (1984) Contribution à l'étude hydrobiologique des lacs salés du sud de l'Altiplano bolivien. *Revue d'Hydrobiologie Tropicale* **17**(3), 259-273.
Javoy M., Pineau F. and Delorme H. (1986) Carbon and nitrogen isotopes in the mantle. *Chemical Geology* **57**(1-2), 41-62.

1014 Jones B. and Renaut R. W. (1994) Crystal fabrics and microbiota in large pisoliths from
1015 Laguna Pastos Grandes, Bolivia. *Sedimentology* **41**(6), 1171-1202.
1016 Kaiser J. F. (2014) Understanding large resurgent calderas and associated magma
1017 systems: the Pastos Grandes Caldera Complex, southwest Bolivia. PhD thesis of Oregon
1018 State University.
1019 Kaiser J. F., de Silva S., Schmitt A. K. Economos R. and Sunagua M. (2017) Million-
1020 year melt–presence in monotonous intermediate magma for a volcanic–plutonic
1021 assemblage in the Central Andes: contrasting histories of crystal-rich and crystal-poor
1022 super-sized silicic magmas. *Earth and Planetary Science Letters* **457**, 73-86.
1023 Kay S. M. and Coira B. L. (2009) Shallowing and steepening subduction zones,
1024 continental lithospheric loss, magmatism, and crustal flow under the Central Andean
1025 Altiplano-Puna Plateau. Backbone of the Americas: shallow subduction, plateau uplift,
1026 and ridge and terrane collision, 204, 229.
1027 Kharaka Y. K., Lico M. S. and Law L. M. (1982) Chemical geothermometers applied to
1028 formation waters, Gulf of Mexico and California basins. *AAPG Bulletin* **66**(5), 588-588.
1029 Kharaka Y. K. and Mariner R. H. (1989) Chemical geothermometers and their
1030 application to formation waters from sedimentary basins. In *Thermal history of*
1031 *sedimentary basins*. Springer, New York, NY. pp. 99-117.
1032 Kussmaul S., Hörmann P. K., Ploskonka E. and Subieta T. (1977) Volcanism and
1033 structure of southwestern Bolivia. *Journal of Volcanology and Geothermal Research*
1034 **2**(1), 73-111.
1035 Lemarchand D., Gaillardet J., Göpel C., Manhès G. (2002) An optimized procedure for
1036 boron separation and mass spectrometry analysis for river samples. *Chemical Geology*
1037 **182**, 323-334.
1038 Li L., Cartigny P. and Ader M. (2009) Kinetic nitrogen isotope fractionation associated
1039 with thermal decomposition of NH3: Experimental results and potential applications to
1040 trace the origin of N_2 in natural gas and hydrothermal systems. *Geochimica et*
1041 *Cosmochimica Acta* **73**(20), 6282-6297.
1042 Louvat P., Moureau J., Paris G., Bouchez J., Noireaux J., Gaillardet J. (2014) A fully
1043 automated direct injection nebulizer (d-DIHEN) for MC-ICP-MS isotope analysis:
1044 application to boron isotope ratio measurements. *Journal of Analytical Atomic*
1045 *Spectrometry* **29**(9), 1698-1707.
1046 Lowenstern J. B. (2001) Carbon dioxide in magmas and implications for hydrothermal
1047 systems. *Mineralium Deposita* **36**(6), 490-502.
1048 Ludington S., Orris G.J., Cox D.P., Long K.R. and Asher-Bolinden S. (1975) Mineral
1049 deposit models. In *Geology and Mineral Resources of the Altiplano and the Cordillera*
1050 *Occidental, Bolivia* (eds Bleiwas D. J. and Christiansen R. G.). U.S. Geol. Survey Bull.
1051 pp. 63-224.
1052 Luddington S., Orris G.J., Cox D.P., Long K.R. and Asher-Bolinder S. (1992) Mineral
1053 deposit models. In *Geology And Mineral Resources Of The Altiplano and Cordillera*
1054 *Occidental, Bolivia* (eds by U.S. Geological Survey and Servicio Geolbgico de Bolivia).
1055 Bull. US geol. Surv. 1975, pp. 63-89.
1056 Marty B. and Jambon A. (1987) ^{3}He in volatile fluxes from the solid Earth: Implications
1057 for carbon geodynamics. *Earth Planetary Science Letter* **83**, 16-26.
1058 McArthur J. M., Kennedy W. J., Chen M., Thirlwall M. F. and Gale A. S. (1994)
1059 Strontium isotope stratigraphy for Late Cretaceous time: direct numerical calibration of
1060 the Sr isotope curve based on the US Western Interior. *Palaeogeography,*
1061 *Palaeoclimatology, Palaeoecology* **108**(1-2), 95-119.

Millot R., Guerrot C. and Vigier N. (2004) Accurate and high-precision measurement of lithium isotopes in two reference materials by MC-ICP-MS. *Geostandards and Geoanalytical Research* **28**(1), 153-159.
Millot R., Scaillet B. and Sanjuan B. (2010) Lithium isotopes in island arc geothermal systems: Guadeloupe, Martinique (French West Indies) and experimental approach. *Geochimica et Cosmochimica Acta* **74**, 1852-1871.
Moquet J. S., Crave A., Viers J., Seyler P., Armijos E., Bourrel L., Chavarri E.N, Lagane C., Laraque A., Lavado Casimiro W.S., Pombosa R., Noriega L., Vera A. and Guyot J.L. (2011) Chemical weathering and atmospheric/soil CO_2 uptake in the Andean and Foreland Amazon basins. *Chemical Geology* **287**(1-2), 1-26.
Moreira M., Rouchon V., Muller E. and Noirez S. (2018) The xenon isotopic signature of the mantle beneath Massif Central. *Geochemical Perspectives Letters* **6**, 28-32.
Moriguti, T., and Nakamura, E. (1998) Across-arc variation of Li isotopes in lavas and implications for crust/mantle recycling at subduction zones. *Earth and planetary science letters* **163**(1-4), 167-174.
Morris R.V., Ruff S.W., Gellert R., Ming D.W., Arvidson R.E., Clark B.C., Golden C.C., Siebach K., Klingelhöfer G., Schröder C., Fleischer I., Yen A.S. and Squyres W. (2010) Identification of carbonate-rich outcrops on Mars by the Spirit rover. *Science* **1189667**.
Morteani G., Möller P., Dulski P. and Preinfalk C. (2014) Major, trace element and stable isotope composition of water and muds precipitated from the hot springs of Bolivia: Are the waters of the spring's potential ore forming fluids? *Chemie der Erde-Geochemistry* **74**(1), 49-62.
Nier A. O. (1950) A redetermination of the relative abundances of the isotopes of carbon, nitrogen, oxygen, argon and potassium. *Physical Review* **77**(6), 789-793.
Ozima M. and Podosek F. A. (2002) *Noble Gas Geochemistry*. Cambridge University Press.
Pace A., Bourillot R., Bouton A., Vennin E., Braissant O., Dupraz C., Duteil T., Bundeleva I., Patrier P., Galaup S., Yokoyama Y., Franceschi M., Virgone A. and Visscher P.T. (2018) Formation of stromatolite lamina at the interface of oxygenic–anoxygenic photosynthesis. *Geobiology* **16**(4), 378-398.
Parkhurst D.L. and Appelo C.A.J. (2013) Description of input and examples for PHREEQC version 3 – a computer program for speciation, batch-reaction, one-dimensional transport, and inverse geochemical calculations. U.S. geological survey techniques and methods, book 6, chap. A43, pp 497.
Pierret M. C., Clauer N., Bosch D., Blanc G. and France-Lanord C. (2001). Chemical and isotopic ($^{87}Sr/^{86}Sr$, $\delta^{18}O$, δD) constraints to the formation processes of Red-Sea brines. *Geochimica et Cosmochimica Acta* **65**(8), 1259-1275.
Pin C. and Bassin C. (1992) Evaluation of a strontium-specific extraction chromatographic method for isotopic analysis in geological materials. *Analytica Chimica Acta* **269**(2), 249-255.
Pineau F. and Javoy M. (1983) Carbon isotopes and concentrations in mid-Atlantic ridge basalts. *Earth Planetary Science Letter* **29**, 413-421.
Pistiner J.S. and Henderson G.M. (2003) Lithium-isotope fractionation during continental weathering processes. *Earth Planetary Science Letter* **214** (1–2), 327-339.
von Strandmann, P. A. P., Burton, K. W., James, R. H., van Calsteren, P., Gíslason, S. R., and Mokadem, F. (2006). Riverine behaviour of uranium and lithium isotopes in an actively glaciated basaltic terrain. *Earth and Planetary Science Letters* **251**(1-2), 134-147.

1110 Richter D. H., Luddington S. and Soria-Escalante E. (1992) Geologic setting. In Geology
1111 and mineral resources of the Altiplano and Cordillera Occidental, Bolivia (eds by U.S.
1112 Geological Survey and Servicio Geolbgico de Bolivia), US. geol. Surv. Bull., 1975, 14-
1113 24.
1114 Risacher F. (1978) Le cadre géochimique des bassins à évaporites des Andes boliviennes.
1115 Cahiers ORSTOM. *Série Géologie* **10**(1), 37-48.
1116 Risacher F. and Eugster H. P. (1979) Holocene pisoliths and encrustations associated
1117 with spring-fed surface pools, Pastos Grandes, Bolivia. *Sedimentology* **26**(2), 253-270.
1118 Risacher F. and Fritz B. (1991) Geochemistry of Bolivian salars, Lipez, southern
1119 Altiplano: origin of solutes and brine evolution. *Geochimica et Cosmochimica Acta*
1120 **55**(3), 687-705.
1121 Risacher F., and Alonso H. (2001) Geochemistry of ash leachates from the 1993 Lascar
1122 eruption, northern Chile. Implication for recycling of ancient evaporites. *Journal of*
1123 *volcanology and geothermal research* **109**(4), 319-337.
1124 Risacher F. and Fritz B. (2009) Origin of salts and brine evolution of Bolivian and
1125 Chilean salars. *Aquatic Geochemistry* **15**(1-2), 123-157.
1126 Risacher F., Alonso H. and Salazar C. (2003) The origin of brines and salts in Chilean
1127 salars: a hydrochemical review. *Earth-Science Reviews* **63**(3-4), 249-293.
1128 Risacher F., Fritz B. and Hauser A. (2011) Origin of components in Chilean thermal
1129 waters. *Journal of South American Earth Sciences* **31**(1), 153-170.
1130 Rissmann C., Leybourne M., Benn C. and Christenson B. (2015) The origin of solutes
1131 within the groundwaters of a high Andean aquifer. *Chemical Geology* **396**, 164-181.
1132 Roche M.A., Fernandez Jauregui C., Aliaga A., Bourges J., Cortes J., Guyot J.L., Pena J.
1133 and Rocha N. (1991) Water and salt balances of the Bolivian amazon (Eds. Braga B.P.F.,
1134 Fernandez Jauregui C.). UNESCO, Manaus, pp. 83–94.
1135 Rosner M., Erzinger J., Franz G. and Trumbull R.B. (2003) Slab- derived boron isotope
1136 signatures in arc volcanic rocks from the Central Andes and evidence for boron isotope
1137 fractionation during progressive slab dehydration. *Geochemistry, Geophysics,*
1138 *Geosystems* **4**, 1–25.
1139 Rothstein D.A. and Manning C.E. (2003) Geothermal gradients in continental magmatic
1140 arcs: Constraints from the eastern Peninsular Ranges batholith, Baja California, México.
1141 In *Tectonic evolution of northwestern México and the southwestern USA: Boulder,*
1142 *Colorado* (eds. Johnson S.E. et al.) *Geological Society of America Special Paper* **374**, pp.
1143 337–354.
1144 Rouchon V., Courtial X., Durand I., Garcia B., Creon L. and Mougin P. (2016) A Fluid
1145 Phase
1146 Equilibria Model in the System CO_2-N_2-H_2O-NaCl-He-Ne-Ar Below 200 Bar and 150°C
1147 – Application to CO_2/He Fractionation in Continental Mantle Degassing. Goldschmidt
1148 Abstracts 2658.
1149 Ryu J. S., Vigier N., Lee S. W., Lee K. S. and Chadwick O. A. (2014) Variation of
1150 lithium isotope geochemistry during basalt weathering and secondary mineral
1151 transformations in Hawaii. *Geochimica et Cosmochimica Acta* **145**, 103-115.
1152 Salisbury M. J., Jicha B. R., de Silva S. L., Singer B. S., Jiménez N. C., and Ort M. H.
1153 (2011) $^{40}Ar/^{39}Ar$ chronostratigraphy of Altiplano-Puna volcanic complex ignimbrites
1154 reveals the development of a major magmatic province. Bulletin, 123(5-6), 821-840.
1155 Sanford W.E. and Wood W.W. (1991) Brine evolution and mineral deposition in
1156 hydrologically open evaporite basins. *American Journal of Science* **291**, 687-710.

Sano Y. and Marty B. (1995) Origin of carbon in fumarolic gas from island arcs. *Chemical Geology* **119**(1-4), 265-274.
Sano Y., Takahata N., Nishio Y. and Marty B. (1998) Nitrogen recycling in subduction zones. *Geophysical Research Letters* **25**, 2289-2292.
Santoyo E., and Díaz-González L. (2010) A new improved proposal of the Na/K geothermometer to estimate deep equilibrium temperatures and their uncertainties in geothermal systems. Proceedings World Geothermal Congress, Bali, Indonesia.
Servant-Vildary S. and Roux M. (1990) Multivariate analysis of diatoms and water chemistry in Bolivian saline lakes. In: *Saline Lakes*. Springer, Dordrecht, pp. 267-290.
Sanjuan B., Millot R., Ásmundsson R., Brach M. and Giroud N. (2014) Use of two new Na/Li geothermometric relationships for geothermal fluids in volcanic environments. *Chemical Geology* **389**, 60-81.
Smith H.J., Spivack A.J., Staudigel H., and Hart S.R. (1995) The boron isotopic composition of altered oceanic crust. *Chemical Geology* **126**, 119–135.
Spiro B., Hoke L. and Chenery C. (1997) Carbon-isotope characteristics of CO_2 and CH_4 in geothermal springs from the Central Andes. *International geology review* **39**(10), 938-947.
Springer M., and Förster, A. (1998). Heat-flow density across the central Andean subduction zone. *Tectonophysics* **291**, 123-139.
Stallard R. F. and Edmond J. M. (1981). Geochemistry of the Amazon: 1. Precipitation chemistry and the marine contribution to the dissolved load at the time of peak discharge. *Journal of Geophysical Research: Oceans* **86**(C10), 9844-9858.
Strauss H. (1997) The isotopic composition of sedimentary sulfur through time. *Palaeogeography, Palaeoclimatology, Palaeoecology* **132**(1-4), 97-118.
Taylor B. E. (1986) Magmatic volatiles: isotopic variations of C, H and S stable isotopes in high temperature geological processes. Reviews in Mineralogy 16 (eds. Valley J. W., Taylor H. P. and O'Neil J. R.) Mineral. Soc. America, pp. 185–225.
Teboul P. A., Durlet C., Gaucher E. C., Virgone A., Girard J. P., Curie J., ... and Camoin G. F. (2016) Origins of elements building travertine and tufa: New perspectives provided by isotopic and geochemical tracers. *Sedimentary Geology* **334**, 97-114.
Teboul P. A. (2017) Diagenesis of lower Cretaceous presalt continental carbonates from the West African margin: simulations and analogues (Doctoral dissertation, Aix-Marseille).
Terra G.J.S., Spadini A.R., França A.B., Sombra C.L., Zambonato E.E., da Silva Juschaks L.C., Arienti L.M., Erthal M.M., Blauth M., Franco M.P., Matsuda N.S., da Silva N.G.C., Moretti Junior P.A., D'Avila R.S.F., de Souza R.S., Tonietto S.N., Couto dos Anjos S.M., Campinho V.S. and Winter W.R. (2010) Classificação de rochas carbonáticas aplicável às bacias sedimentares brasileiras. *Bulletin Geoscience Petrobras, Rio de Janeiro* **18** (1), 9–29
Thorpe R. S., Potts P. J., and Francis P. W. (1976) Rare earth data and petrogenesis of andesite from the North Chilean Andes. *Contributions to Mineralogy and Petrology* **54**(1), 65-78.
Tosca N.J., Wright V.P. (2015) Diagenetic pathways linked to labile Mg-clays in lacustrine carbonate reservoirs: a model for the origin of secondary porosity in the Cretaceous Pre-salt Barra Velha Formation, Offshore Brazil, 435. Geological Society of London, Special Publication. SP435-1.

1203 Verkouteren R. M. and Klinedinst D. B. (2004) Value Assignment and Uncertainty
1204 Estimation of Selected Light Stable Isotope Reference Materials: RMs 8543-8545, RMs
1205 8562-8564, and RM 8566. *NIST Special Publication* **260** (149), 59.
1206 Verma S. P. and Santoyo E. (1995) New improved equations for Na/K and SiO_2
1207 geothermometers by error propagation. *Proc. World Geotherm. Congr* **2**, 963-968.
1208 Verma, S. P. and Santoyo E. (1997) New improved equations for Na/K, Na/Li and SiO_2
1209 geothermometers by outlier detection and rejection. *Journal of Volcanology and*
1210 *Geothermal Research* **79**(1-2), 9-23.
1211 Verrecchia E.P. (2007) Lacustrine and palustrine geochemical sediments - Chapter 9. In:
1212 Terrestrial geochemical sediments and geomorphology (Eds. D.J. Nash and S.J.
1213 McLaren), Blackwell, London, Oxford, pp. 298-329.
1214 Weinlich F. H., Bräuer K., Kämpf H., Strauch G., Tesař J. and Weise S. M. (1999) An
1215 active subcontinental mantle volatile system in the western Eger rift, Central Europe: Gas
1216 flux, isotopic (He, C, and N) and compositional fingerprints. *Geochimica et*
1217 *Cosmochimica Acta* **63**(21), 3653-3671.
1218 Zamanian K., Pustovoytov K. and Kuzyakov Y. (2016). Pedogenic carbonates: Forms
1219 and formation processes. *Earth-Science Reviews* **157**, 1-17.
1220 Zimmer M. M., Fischer T. P., Hilton D. R., Alvarado G. E., Sharp Z. D. and Walker J. A.
1221 (2004). Nitrogen systematics and gas fluxes of subduction zones: insights from Costa
1222 Rica arc volatiles. *Geochemistry, Geophysics, Geosystems* **5**(5).
1223

Figure Captions

Fig. 1: **a.** Topographic map of Central Andes showing the location of Laguna Pastos Grandes among the main Chilean and Bolivian salars (in white); **b.** Zoom into the geological context of Laguna Pastos Grandes (modified from Bougeault et al., 2019); satellite image provided by Zoom Earth website, © 2018 Microsoft Corporation Earthstar Geographics SIO; **c.** View of the carbonate platform with partially immerged calcitic pisoliths.

Fig. 2: Location of water and gas sampling in streams (blue stars), thermal springs (red stars) and of the brine in one of the sustainable lakes (yellow star) in Laguna Pastos Grandes (Bolivia). The location of volcanic rock samples is also shown with black dots. The four thermal springs (images 1-4) flow up through the recent carbonate platform developing at the west of the laguna. The arrows point to the bubbling gas in water basins, except for "El Gigante" where gas and water have separate vents. Ign.: Ignimbrite; Dac.: Dacite; And.: Andesite.

Fig. 3: Relative abundance of air-normalized isotope composition of noble gas (^{4}He, ^{20}Ne, ^{36}Ar, $^{40}Ar/^{36}Ar$ and $^{3}He/^{4}He$) in thermal springs El Ojo Verde, La Rumba, La Salsa and El Gigante. Normalization values used as references are 295.5 for $^{40}Ar/^{36}Ar$ ratio (Nier, 1950) and $1.39x10^{-6}$ for $^{3}He/^{4}He$ ratio (Ozima and Podosek, 2002). Helium isotope ratios are corrected for the effects of ASW (Air saturated Water) contamination in hydrothermal system and are equivalent to Rc/Ra.

Fig. 4: Plot of $\delta^{18}O$ versus $\delta^{2}H$ for Pastos Grandes waters. Plot b is focused on thermal springs (in red) and cold streams (in blue) in comparison with a rainfall sample (in white) collected at the same altitude during the wet season in March 2017. Two samples of snow (grey) were also collected during the dry season in January 2016. Data of rainfall and snow are presented in Table A2. The composition of the lake brine (in yellow) of Pastos Grandes is compared with the other Andean salars (in black, from this study and Boschetti et al., 2007; Table A2). The Local Meteoric Water Line (LMWL; Chaffaut et al., 1998) and the Local Ground- and Spring-Water Line (LGSWL; Rissmann et al., 2015) for the South-Central Andes are also shown.

Fig. 5: Chemical compositions of Laguna Pastos Grandes water sources (thermal springs in red/orange and streams in blue) and lake brine (in yellow). **a.** Schoeller diagram showing relative concentrations in solutes; **b.** Plot of Ca versus Alkalinity (mM); **c.** Plot of Cl concentration versus Cl/Br. Data from this study are reported with dots and previous data with squares (Ballivian and Risacher, 1981; Hurlbert and Chang, 1984; Risacher and Fritz, 1991; Jones and Renaut, 1994).

Fig. 6: Sr, Li and B isotopic compositions of Laguna Pastos Grandes water sources (thermal springs in red and streams in blue) and lake brine (in yellow) compared with andesite, dacite (this study), and rhyolitic ignimbrite (this study and Kaiser, 2014) from the Pastos Grandes caldera. **a.** $^{87}Sr/^{86}Sr$ vs Sr concentration (mg/l) data compared with Cenomanian-Turonian marine carbonates (McArthur et al., 1994) representing the last marine sedimentary sequence in the central Andes region and modern marine evaporites (Pierret et al., 2001). Mean values in Andean Central Volcanic Zone (CVZ) dacite (D) and andesite

(A) are also shown for comparison (Cortecci et al., 2005); **b.** $\delta^{11}B$ vs $\delta^{7}Li$ data compared with modern seawater (Boschetti et al., 2017) and rocks from the Andean volcanic arc (Chan et al., 2002; Rosner et al., 2003).

Fig. 7: Comparison of the water composition obtained for the volcanic bedrock weathering at 200 (blue), 225 (red) and 250 °C (green) with increasing pCO_2 from 10 bar in light color to 100 bar in dark color. The average spring water is in black.

Fig. 8: Conceptual model of modern carbonate precipitation in relation to the sources of water and gas in Laguna Pastos Grandes. Violet-blue arrows refer to hydrothermal circulations. See the conclusion for details. Data for boron isotopes are from De Hoog and Savov (2018) for the Altered Oceanic Crust (AOC) and marine sediments and Marschall (2018) for the mantle. Data for lithium isotopes are from Chan and Kastner (2000) for subducted sediments, Moriguti and Nakamura (1998) and Chan et al. (1992) for AOC and Misra et al. (2012) for the mantle. Data for nitrogen isotopes are from Ader et al. (2016) for sediments and Sano et al. (1998) for the crust. Data for carbon isotopes are from Hoefs (1980) for sedimentary organic carbon and Pineau and Javoy (1983) for mantle-derived signature. Rc/Ra data are from Hoke et al (1994). Other data are from this study.

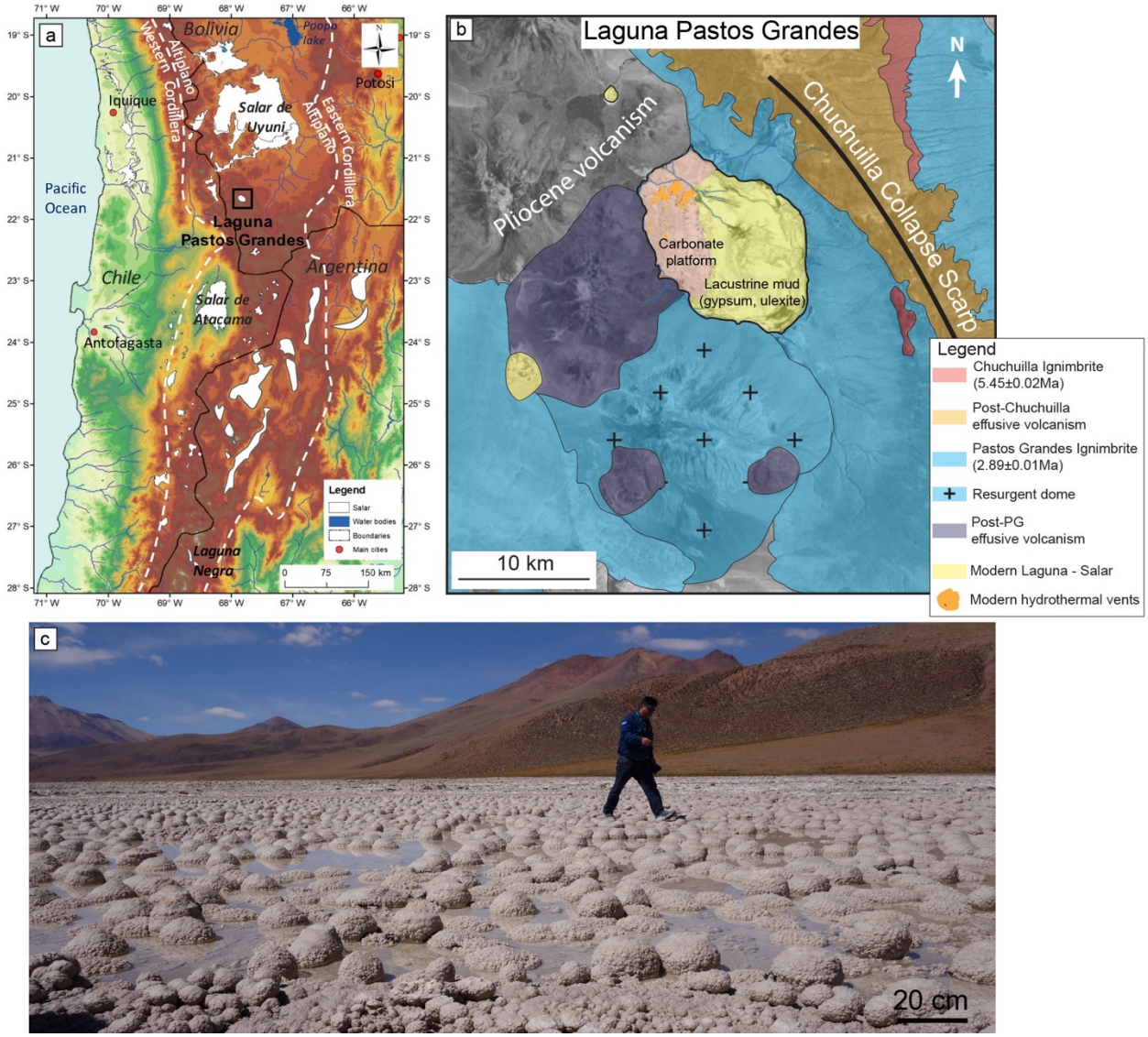
a
Bolivia
Poopo lake
Western Cordillera
Altiplano
Eastern Cordillera
Altiplano
Iquique
Salar de Uyuni
Potosi
Pacific Ocean
Laguna Pastos Grandes
Chile
Argentina
Salar de Atacama
Antofagasta
Laguna Negra
Legend
Salar
Water bodies
Boundaries
Main cities
0 75 150 km
b
Laguna Pastos Grandes
N
Pliocene volcanism
Chuchuilla Collapse Scarp
Carbonate platform
Lacustrine mud (gypsum, ulexite)
10 km
Legend
Chuchuilla Ignimbrite (5.45±0.02Ma)
Post-Chuchuilla effusive volcanism
Pastos Grandes Ignimbrite (2.89±0.01Ma)
Resurgent dome
Post-PG effusive volcanism
Modern Laguna - Salar
Modern hydrothermal vents
c
20 cm

Figure 1.

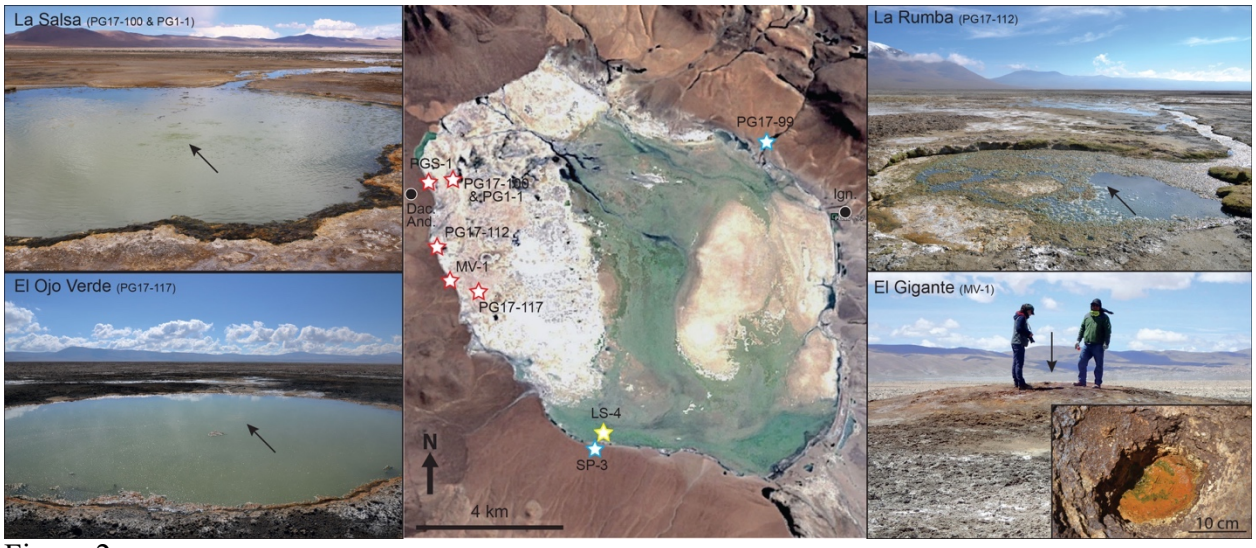
La Salsa (PG17-100 & PG1-1)
El Ojo Verde (PG17-117)
PG17-99
RGS-1
PG17-109
&PG1-1
Dac.
And.
PG17-112
MV-1
PG17-117
Ign.
LS-4
SP-3
N
4 km
La Rumba (PG17-112)
El Gigante (MV-1)
10 cm

Figure 2.

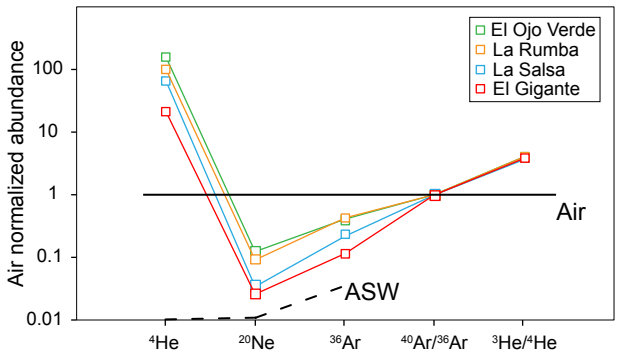
El Ojo Verde
La Rumba
La Salsa
El Gigante
Air normalized abundance
100
10
1
0.1
0.01
Air
ASW
4He
20Ne
36Ar
40Ar/36Ar
3He/4He

Figure 3.

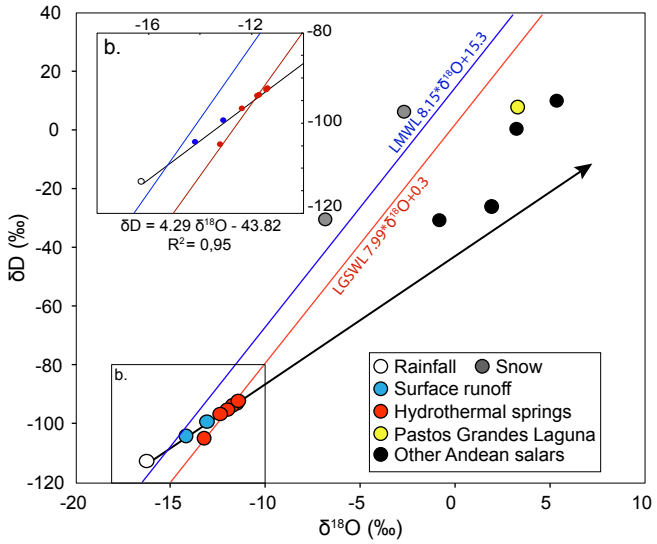
δD = 4.29 δ18O - 43.82
R2= 0,95
LMWL 8.15*δ18O+15.3
LGSWL 7.99*δ18O+0.3
Rainfall
Snow
Surface runoff
Hydrothermal springs
Pastos Grandes Laguna
Other Andean salars
δD (‰)
δ18O (‰)

Figure 4.

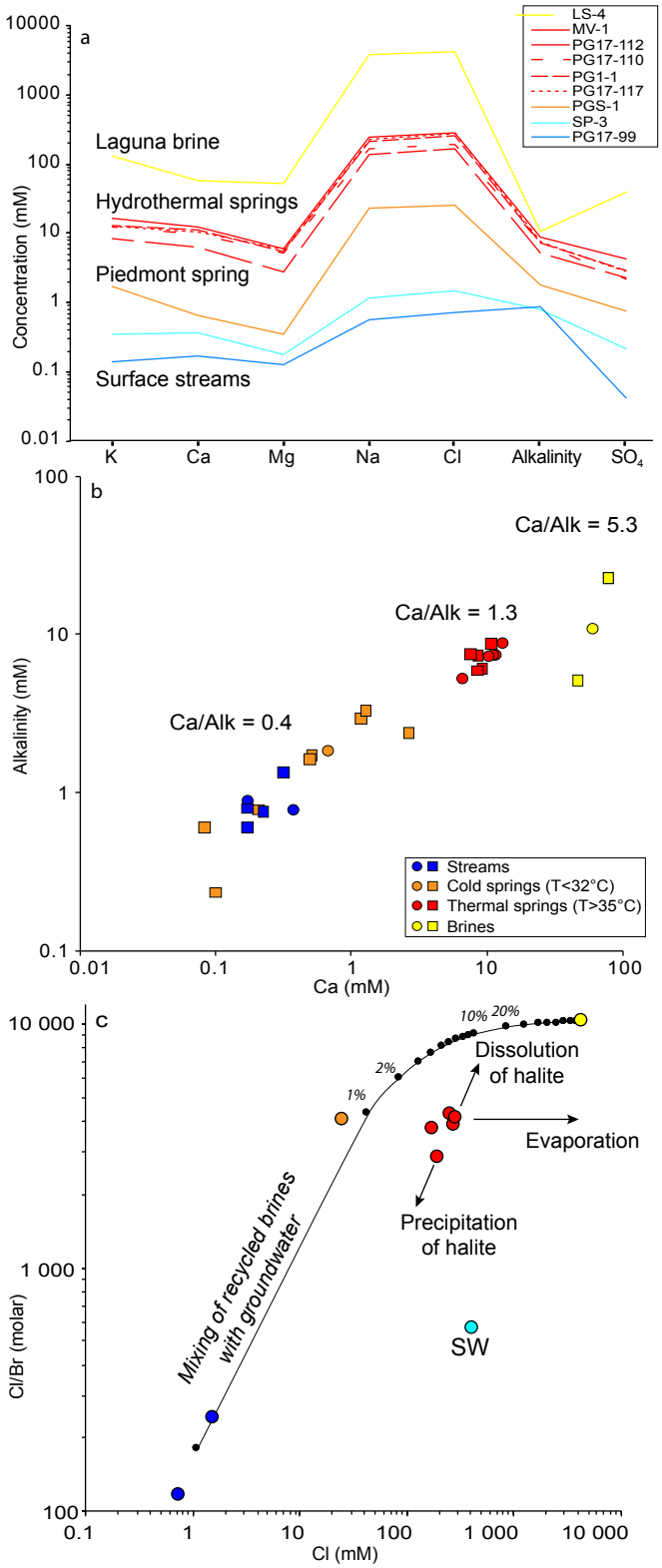
a
LS-4
MV-1
PG17-112
PG17-110
PG1-1
PG17-117
PGS-1
SP-3
PG17-99
Laguna brine
Hydrothermal springs
Piedmont spring
Surface streams
Concentration (mM)
10000
1000
100
10
1
0.1
0.01
K
Ca
Mg
Na
Cl
Alkalinity
SO4
b
Ca/Alk = 5.3
Ca/Alk = 1.3
Ca/Alk = 0.4
Alkalinity (mM)
Streams
Cold springs (T<32°C)
Thermal springs (T>35°C)
Brines
Ca (mM)
c
10%
20%
2%
1%
Dissolution
of halite
Evaporation
Precipitation
of halite
Mixing of recycled brines
with groundwater
SW
Cl/Br (molar)
10 000
1 000
100
Cl (mM)

Figure 5.

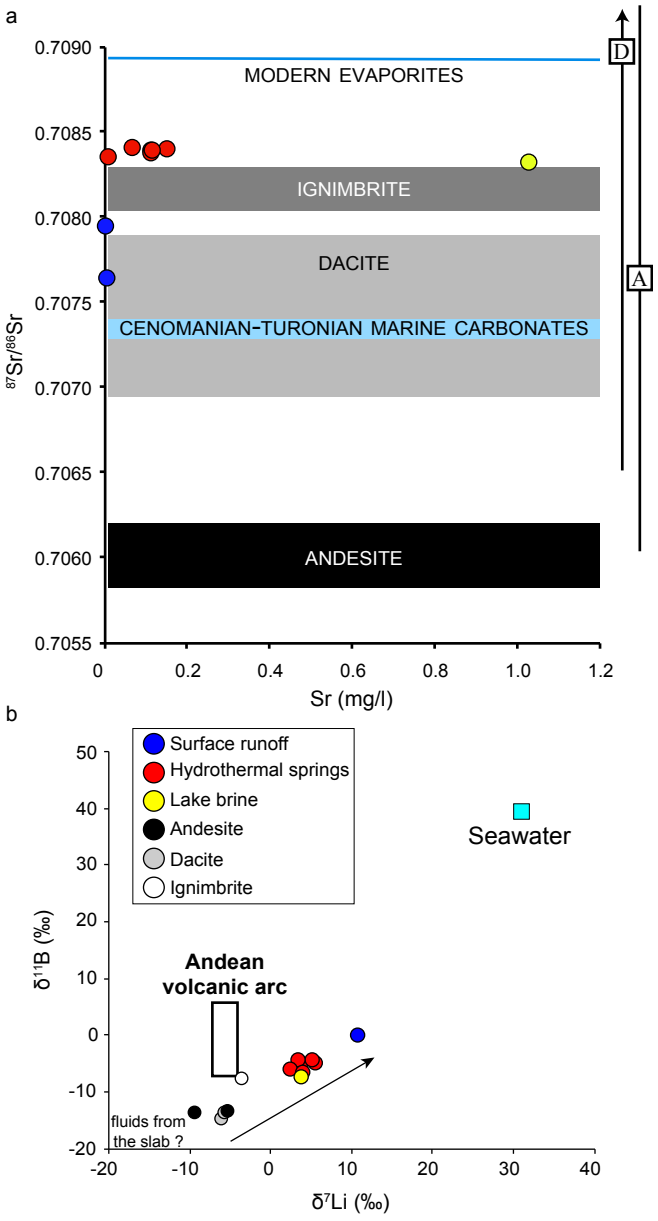
a
0.7090
0.7085
0.7080
0.7075
0.7070
0.7065
0.7060
0.7055
87Sr/86Sr
MODERN EVAPORITES
IGNIMBRITE
DACITE
CENOMANIAN-TURONIAN MARINE CARBONATES
ANDESITE
D
A
0
0.2
0.4
0.6
0.8
1.0
1.2
Sr (mg/l)
b
Surface runoff
Hydrothermal springs
Lake brine
Andesite
Dacite
Ignimbrite
Seawater
Andean
volcanic arc
fluids from
the slab ?
δ11B (‰)
δ7Li (‰)
50
40
30
20
10
0
-10
-20
-20
-10
0
10
20
30
40

Figure 6.

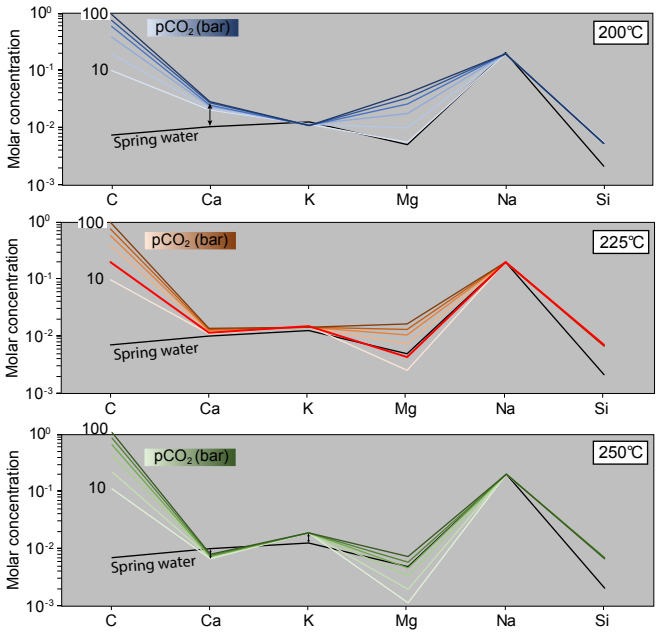
Molar concentration
10^0
10^{-1}
10^{-2}
10^{-3}
100
10
pCO_2 (bar)
200℃
Spring water
C
Ca
K
Mg
Na
Si
225℃
250℃

Figure 7.

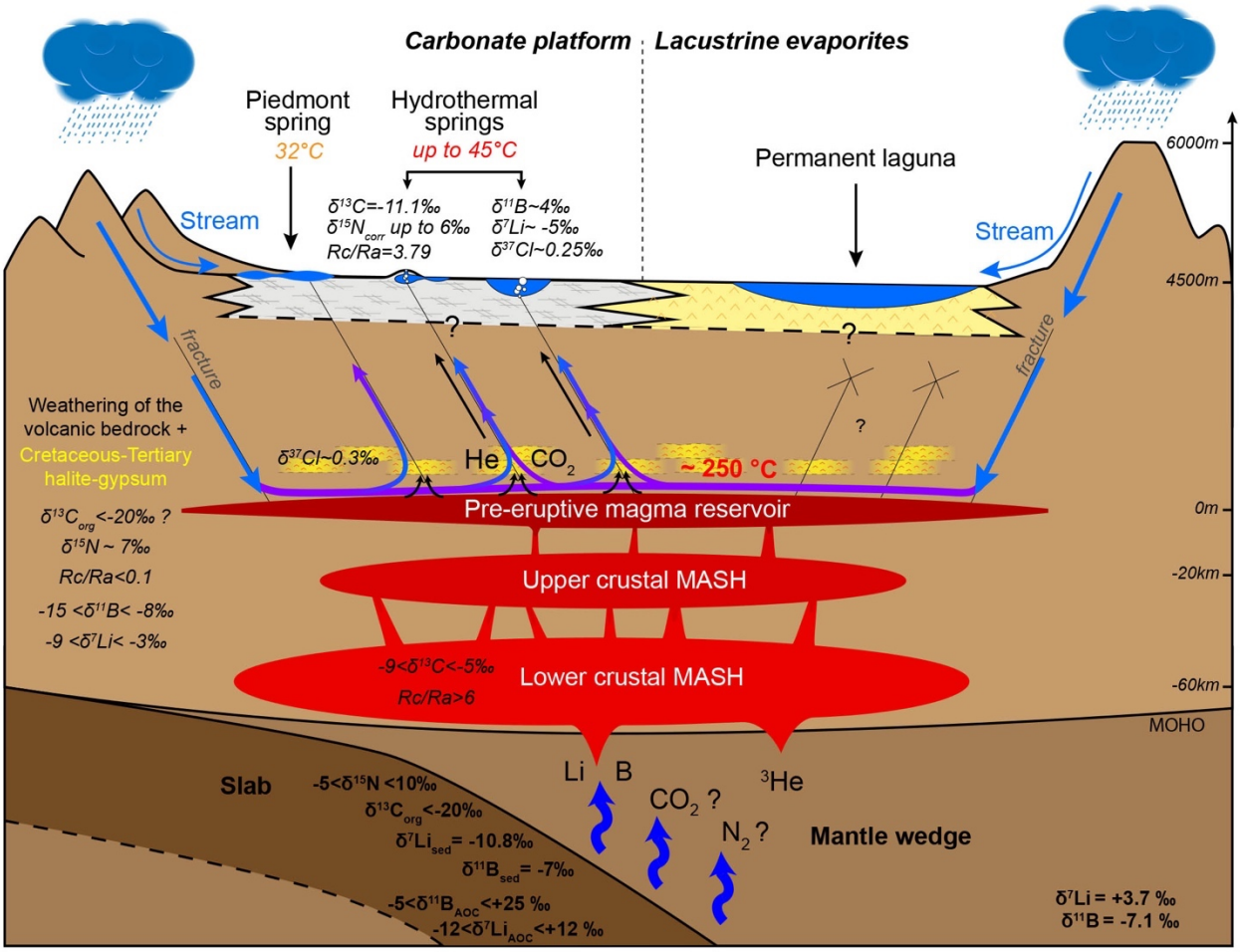
Carbonate platform
Lacustrine evaporites
Piedmont spring
32°C
Hydrothermal springs
up to 45°C
Permanent laguna
Stream
Stream
δ13C=-11.1‰
δ15Ncorr up to 6‰
Rc/Ra=3.79
δ11B~4‰
δ7Li~ -5‰
δ37Cl~0.25‰
6000m
4500m
0m
-20km
-60km
MOHO
fracture
fracture
Weathering of the volcanic bedrock + Cretaceous-Tertiary halite-gypsum
δ13Corg<-20‰ ?
δ15N ~ 7‰
Rc/Ra<0.1
-15 <δ11B< -8‰
-9 <δ7Li< -3‰
δ37Cl~0.3‰
He
CO2
~ 250 °C
Pre-eruptive magma reservoir
Upper crustal MASH
-9<δ13C<-5‰
Rc/Ra>6
Lower crustal MASH
Slab
-5<δ15N <10‰
δ13Corg<-20‰
δ7Lised= -10.8‰
δ11Bsed= -7‰
-5<δ11BAOC<+25 ‰
-12<δ7LiAOC<+12 ‰
Li
B
CO2 ?
3He
N2 ?
Mantle wedge
δ7Li = +3.7 ‰
δ11B = -7.1 ‰

Figure 8.

Supplementary Material

PHREEQC modeling:

The mineralogical composition of the volcanic rocks sampled around the Laguna Pastos has been determined by DRX as:

- Dacite: alkali and potassium feldspar, quartz, biotite
- Andesite: alkali feldspar, biotite, olivine, amphibole
- Ignimbrite: alkali and potassium feldspar, quartz, biotite, amphibole

As numerous of these minerals are not available in the Thermoddem database, we performed the PHREEQC modeling with the selected minerals as follows:

```
Solution 1
units mmol/l
temp    225 # Temperature varying between 200 and 250 °C
Equilibrium_phases 1
        Quartz(alpha) 0.0     10.0
        Sanidine      0.0     10.0
        Albite(low)   0.0     10.0
        Anorthite     0.0     10.0
        Pargasite     0.0     10.0
        Anhydrite     0.0     10.0
        CO2(g)        1.3             #CO2(g) SI varying between 1-2
        Halite        0.0     0.239   #Corresponding to the average Cl concentration in
End                                   spring water
```

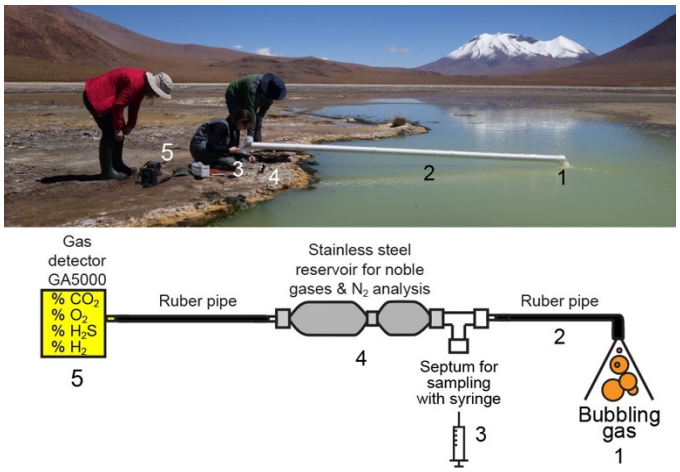

1339

1340 **Figure A1.** Photography and illustrating schema of bubbling gas sampling method.

1341

1342

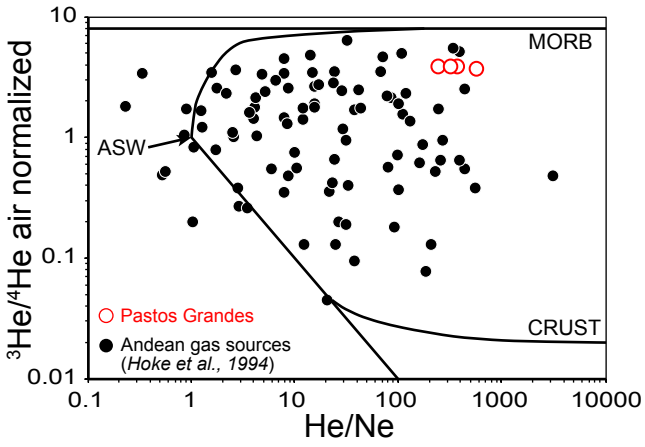

1343

1344 **Figure A2.** Air-normalized helium R/Ra values plotted against He/Ne ratios of gas samples
1345 from Laguna Pastos Grandes compared with other Andean sources (Hoke et al., 1994).

Mixing lines between the three main sources of helium (crustal CRUST, mantle MORB and air saturated water ASW) are also represented.

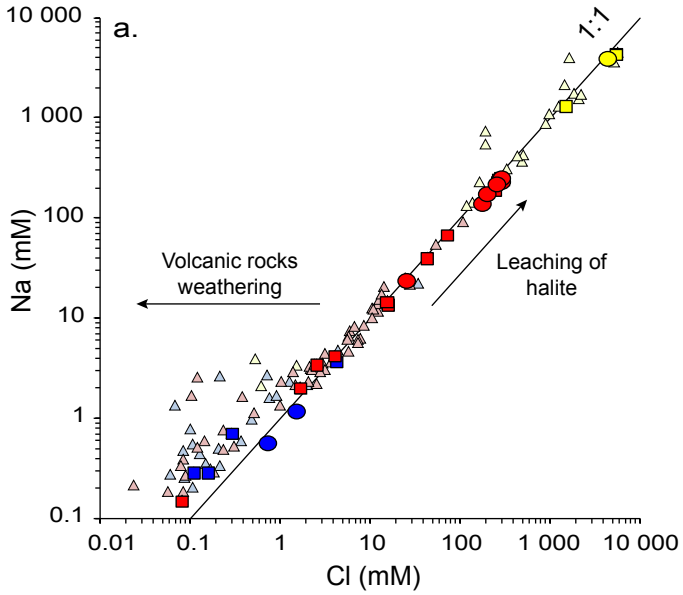

Figure A3. Relations between chloride and sodium for Pastos Grandes brines (in yellow) and water sources as a function of temperature: thermal spring >35 °C in red, <32 °C in orange and cold stream <15 °C in blue. Na-Cl compositions are compared with other Bolivian salars (pale triangles; Risacher and Fritz, 1991). Data from this study are reported with dots and previous data with squares (Ballivian and Risacher, 1981; Hurlbert and Chang, 1984; Risacher and Fritz, 1991; Jones and Renaut, 1994).

Table A1. Detailed nitrogen and carbon isotopic analysis of gas samples from Laguna Pastos Grandes.

Nitrogen analysis				
Sample	Date	Method	$\delta^{15}N$ (‰)	1σ
PG100	20/07/2017	GC-IRMS on steel tube	2.73	0.03
PG100	20/07/2017	GC-IRMS on steel tube	2.75	0.01
PG112	20/07/2017	GC-IRMS on steel tube	1.79	0.02
PG112	20/07/2017	GC-IRMS on steel tube	1.77	0.01
PG112	07/02/2018	GC-IRMS on exetainer	1.74	0.02
PG116	07/02/2018	GC-IRMS on exetainer	1.60	0.02
PG117	19/07/2017	GC-IRMS on steel tube	2.49	0.05
PG117	19/07/2017	GC-IRMS on steel tube	2.47	0.03
PG117	19/07/2017	GC-IRMS on steel tube	2.24	0.03
PG117	19/07/2017	GC-IRMS on steel tube	2.26	0.02
PG117	19/07/2017	GC-IRMS on steel tube	2.18	0.02
PG117	19/07/2017	GC-IRMS on steel tube	2.17	0.02

Carbon analysis				
Sample	Date	Method	$\delta^{13}C$ (‰)	1σ
PG100	14/06/2017	GC-C-IRMS	-11.36	0.01
PG100	14/06/2017	GC-C-IRMS	-11.32	0.01
PG100	14/06/2017	GC-C-IRMS	-11.31	0.01
PG100	20/07/2017	GC-IRMS	-10.73	0.03
PG100	20/07/2017	GC-IRMS	-11.27	0.03
PG112	14/06/2017	GC-C-IRMS	-11.31	0.01
PG112	14/06/2017	GC-C-IRMS	-11.24	0.01
PG112	14/06/2017	GC-C-IRMS	-11.26	0.01
PG112	20/07/2017	GC-IRMS	-11.11	0.03
PG112	20/07/2017	GC-IRMS	-11.24	0.03
PG116	14/06/2017	GC-C-IRMS	-11.25	0.03
PG116	14/06/2017	GC-C-IRMS	-11.08	0.03
PG116	14/06/2017	GC-C-IRMS	-11.05	0.03
PG116	07/02/2018	GC-IRMS	-11.00	0.04
PG116	07/02/2018	GC-IRMS	-11.49	0.04
PG116	07/02/2018	GC-IRMS	-11.43	0.06
PG117	14/06/2017	GC-C-IRMS	-11.06	0.04
PG117	19/07/2017	GC-IRMS	-10.85	0.05

1359 **Table A2.** Stable isotope compositions of Andean salars water, rainfall and snow from the
1360 region of Pastos Grandes (from this study* and Boschetti et al., 2007).

	$\delta^{18}O$ (±0.1‰, 1s)	δD (±0.8‰, 1s)
Chaxa lagoon	-0.8	-30.5
Miñique lagoon	5.4	10.1
Miscanti lagoon	3.3	0.5
Uyuni*	1.9	-26.1
Rainfall*	-16.3	-112.9
Snow 1*	-6.8	-30.3
Snow 2*	-2.7	6.5

Table A3. $\delta^{37}Cl$ analyses of water samples from Laguna Pastos Grandes.

Sample	$\delta^{37}Cl$ (‰)	1σ
La Salsa 1	0.308	0.002
La Salsa 2	0.230	0.010
La Salsa 3	0.230	0.009
La Salsa 4	0.260	0.009
La Salsa 5	0.234	0.003
La Salsa 6	0.292	0.002
La Salsa 7	0.300	0.002
La Rumba 1	0.227	0.010
La Rumba 2	0.205	0.006
La Rumba 3	0.234	0.011
El Ojo Verde 1	0.246	0.009
El Ojo Verde 2	0.252	0.013
Average	**0.251**	**0.032**

Table A4. Results of PHREEQC modeling. Alb. Albite(low); Anh. Anhydrite; An. Anorthite; Hal. Halite; Par. Pargasite; Qtz. Quartz(alpha); San. Sanidine

	pCO_2 (bar)	Amount of dissolution (-) or precipitation (+) (molality)								Water chemistry (molality)							
		Alb.	Anh.	An.	CO2(g)	Hal.	Par.	Qtz	San.	C	Ca	Cl	K	Mg	Na	S	Si
Input temperature: 200 °C	10	4.9E-2	-5.0E-4	-1.7E-2	-1.0E-1	-2.4E-1	-1.4E-3	-7.6E-2	-1.1E-2	1.0E-1	2.0E-2	2.4E-1	1.1E-2	5.6E-3	1.9E-1	5.0E-4	5.4E-3
	20	5.0E-2	-5.3E-4	-1.6E-2	-2.0E-1	-2.4E-1	-2.4E-3	-7.6E-2	-1.1E-2	2.0E-1	2.1E-2	2.4E-1	1.1E-2	9.8E-3	1.9E-1	5.3E-4	5.4E-3
	40	5.2E-2	-5.7E-4	-1.4E-2	-3.9E-1	-2.4E-1	-4.4E-3	-7.4E-2	-1.1E-2	3.9E-1	2.3E-2	2.4E-1	1.1E-2	1.8E-2	1.9E-1	5.7E-4	5.4E-3
	60	5.4E-2	-6.0E-4	-1.2E-2	-5.8E-1	-2.4E-1	-6.3E-3	-7.2E-2	-1.1E-2	5.8E-1	2.5E-2	2.4E-1	1.1E-2	2.5E-2	1.9E-1	6.0E-4	5.3E-3
	80	5.5E-2	-6.3E-4	-9.9E-3	-7.6E-1	-2.4E-1	-8.1E-3	-6.9E-2	-1.1E-2	7.6E-1	2.7E-2	2.4E-1	1.1E-2	3.2E-2	1.9E-1	6.3E-4	5.3E-3
	100	5.7E-2	-6.6E-4	-7.8E-3	-9.6E-1	-2.4E-1	-1.0E-2	-6.7E-2	-1.1E-2	9.6E-1	2.9E-2	2.4E-1	1.1E-2	4.0E-2	1.9E-1	6.6E-4	5.3E-3
Input temperature: 225 °C	10	3.6E-2	-4.5E-4	-9.4E-3	-1.0E-1	-2.4E-1	-6.4E-4	-4.7E-2	-1.5E-2	1.0E-1	1.1E-2	2.4E-1	1.5E-2	2.6E-3	2.0E-1	4.5E-4	7.2E-3
	20	3.6E-2	-4.7E-4	-8.9E-3	-2.0E-1	-2.4E-1	-1.1E-3	-4.6E-2	-1.5E-2	2.0E-1	1.2E-2	2.4E-1	1.5E-2	4.4E-3	2.0E-1	4.7E-4	7.1E-3
	40	3.7E-2	-4.9E-4	-8.1E-3	-4.0E-1	-2.4E-1	-1.9E-3	-4.5E-2	-1.5E-2	4.0E-1	1.2E-2	2.4E-1	1.5E-2	7.7E-3	2.0E-1	4.9E-4	7.1E-3
	60	3.7E-2	-5.1E-4	-7.2E-3	-6.0E-1	-2.4E-1	-2.7E-3	-4.4E-2	-1.5E-2	6.0E-1	1.3E-2	2.4E-1	1.5E-2	1.1E-2	2.0E-1	5.1E-4	7.0E-3
	80	3.8E-2	-5.2E-4	-6.3E-3	-7.9E-1	-2.4E-1	-3.4E-3	-4.3E-2	-1.5E-2	7.9E-1	1.4E-2	2.4E-1	1.5E-2	1.4E-2	2.0E-1	5.2E-4	7.0E-3
	100	3.8E-2	-5.4E-4	-5.4E-3	-9.9E-1	-2.4E-1	-4.2E-3	-4.1E-2	-1.5E-2	1.0E0	1.4E-2	2.4E-1	1.5E-2	1.7E-2	2.0E-1	5.4E-4	6.9E-3
Input temperature: 250 °C	10	3.2E-2	-4.3E-4	-5.8E-3	-1.1E-1	-2.4E-1	-3.0E-4	-3.1E-2	-1.9E-2	1.1E-1	6.8E-3	2.4E-1	1.9E-2	1.2E-3	2.1E-1	4.3E-4	7.3E-3
	20	3.2E-2	-4.4E-4	-5.6E-3	-2.2E-1	-2.4E-1	-5.0E-4	-3.1E-2	-1.9E-2	2.2E-1	7.0E-3	2.4E-1	1.9E-2	2.0E-3	2.1E-1	4.4E-4	7.2E-3
	40	3.2E-2	-4.5E-4	-5.2E-3	-4.5E-1	-2.4E-1	-8.6E-4	-3.0E-2	-1.9E-2	4.5E-1	7.3E-3	2.4E-1	1.9E-2	3.5E-3	2.1E-1	4.5E-4	7.2E-3
	60	3.3E-2	-4.6E-4	-4.8E-3	-6.7E-1	-2.4E-1	-1.2E-3	-3.0E-2	-1.9E-2	6.7E-1	7.6E-3	2.4E-1	1.9E-2	4.8E-3	2.1E-1	4.6E-4	7.1E-3
	80	3.3E-2	-4.7E-4	-4.4E-3	-8.8E-1	-2.4E-1	-1.5E-3	-2.9E-2	-1.9E-2	8.9E-1	7.9E-3	2.4E-1	1.9E-2	6.1E-3	2.1E-1	4.7E-4	7.1E-3
	100	3.3E-2	-4.7E-4	-4.0E-3	-1.1E0	-2.4E-1	-1.8E-3	-2.9E-2	-1.9E-2	1.1E0	8.2E-3	2.4E-1	1.9E-2	7.3E-3	2.1E-1	4.7E-4	7.0E-3